Cell Death Characterization in Tumor Constructs Using Irreversible Electroporation

Katherine Jane Prokop

Thesis submitted to the faculty of the Virginia Polytechnic Institute & State University
in partial fulfillment of the requirements for the degree of

Master of Science
In
Biomedical Engineering and Sciences

Rafael V. Davalos
John L. Robertson
Daniela Cimini

August 26, 2013
Blacksburg, VA

Keywords: Irreversible electroporation, hydrogels, pancreatic cancer, prostate cancer

Cell Death Characterization in Tumor Constructs Using Irreversible Electroporation

Katherine Jane Prokop

ABSTRACT

Pancreatic and prostate cancer are both prevalent cancers in the United States with pancreatic being one of the most aggressive of all cancers and prostate cancer being one of the most common, ranking as the number one cancer in men. Treatment of both cancers can be quite challenging as the anatomy of the pancreas and prostate, as well as the development and diagnosis of the disease can greatly limit treatment options. Therefore, it is necessary to develop new cancer treatments to help manage and prevent these cancers.

Irreversible electroporation is a new non-thermal focal ablation therapy utilizing short, pulsed electric fields to damage cell membranes leading to cell death. The therapy is minimally invasive, involving the insertion of needle electrodes into the region of interest and lasts less than two minutes. Heat sink effects that thermal therapies experience near large blood vessels do not affect irreversible electroporation. This allows the treatment to be used on tumors near vasculature as well as critical structures without harming these vital regions.

While irreversible electroporation is a promising new cancer therapy, further developments are necessary to improve treatment planning models. This work aims to further understand the electric field thresholds necessary to kill different types of cancer cells with a focus on pancreatic and prostate cancer. The work is done using an *in vitro* tumor (hydrogel) model as this model is better than traditional cell suspension studies, with added benefits over the immediate use of tissue and animal models.

Acknowledgements

First and foremost, I would like to thank my parents for their constant love and support; I would not be where I am today if it wasn't for you. You've worked so hard and sacrificed so much to give me every opportunity and I am so grateful for that. Many thanks to the rest of my family and friends for their encouragement and support throughout.

In addition, I would like to thank my advisor, Dr. Davalos, for the opportunity to work in this exciting field as well as for his guidance and support throughout my graduate career. Many thanks to Dr. Bob for offering insight and advising the biological aspects of my work, as well as to Dr. Cimini for teaching me the necessary biological skill sets. I am grateful to the IRE group in the Bioelectromechanical Systems (BEMS) lab, especially Chris Arena, Paulo Garcia, and Mike Sano for their mentorship. Thanks to the rest of my lab members for their support and creating a great environment to work in. I would also like to acknowledge the MultiSTEPS Interdisciplinary Graduate Education Program (IGEP) for their financial support.

Table of Contents

List of Figures

List of Tables

Chapter One: Introduction

Pancreatic cancer is one of the deadliest and most aggressive cancers, with the fourth leading death rate among cancers in developed countries [1-3]. In 2013, an estimated 45,220 new cases will be diagnosed with approximately 38,460 of those resulting in death. Pancreatic cancer death rates have been increasing in recent years with most patients succumbing to the disease within the first year of diagnosis and only 6% surviving to five years. Pancreatic cancer often does not present with early symptoms, and therefore, is generally not detected until later stages at which point only about 15-20% of cases are candidates for surgery. Surgery is currently the only option for long-term survival of the disease in which pancreatoduodenectomys (Whipple procedures) and pancreatotectomys are the most common procedures to remove diseased parts of the pancreas, followed by adjuvant therapies such as chemotherapy and radiation therapy. Research is focused on improving early detection techniques as well as new treatment options, including targeted therapy such as irreversible electroporation [1-3]

Prostate cancer is one of the most prevalent cancers in the US with an estimated 238,590 new cases developing in 2013. According to the American Cancer Society 29,720 of these cases will result in death [1, 4]. Prostate cancer is the most frequently diagnosed cancer in men, often not presenting symptoms until more advanced stages, at which time metastasis to bone can occur. While the survival rates for prostate cancer are high compared to many others, with 5 year survival rates of 100% and 93% 15 year survival, new therapies for the disease need to be investigated due to the complicated anatomy. Current treatments include surgery, chemotherapy, radiation therapy, immunotherapy, and vaccine therapy [4], and are often complicated by prostate anatomy making tumors inoperable and increasing the risk of urinary and erectile

dysfunction [1]. New therapies are necessary to eradicate these challenges and improve treatment of cancer not only for prostate and pancreatic but for other cancer's as well.

Irreversible electroporation is a promising non-thermal ablation therapy to treat cancer. Application of short, pulsed electric fields through minimally invasive needle electrodes leads to cell death in the targeted region. Although the therapy has shown great potential in both *in vivo* and beginning phase clinical trials, further developments into understanding the molecular mechanisms behind electroporation, as well as improved treatment planning models are necessary. This work aims to determine the electric field thresholds necessary for cell death for two cancer cells lines, pancreatic and prostate. An *in vitro* tumor construct (hydrogel) is used for these experiments as it offers a more physiological environment than traditional cell suspension studies, allowing cells to attach, while negating the immediate need for animal studies. Additionally, the hydrogel model is a better preliminary model than tissue and animal models as the change in bulk conductivity due to electroporation is difficult to measure in tissue and animal models when also determining the electric field threshold for cell death, and therefore, is generally estimated. The low cell seeding density in the hydrogel assumes the bulk conductivity to be negligible, which allows for a more easily determined electric field threshold that can later be used in tissue and animal models to back out the transient conductivity values due to electroporation for specific tissues. Furthermore, this work will discuss the background and theory behind electroporation in Chapter 2, while Chapter 3 will focus on the methods used to determine cell death thresholds in the tumor constructs. Chapter 4 will explain the results, and Chapter 5 will finish up with the discussion and future work.

Chapter Two: Background and Significance

2.1 Irreversible Electroporation

Electroporation is a technique used to permeabilize the cell membrane through the application of pulsed electric fields (PEF) using electrodes. Application of PEF increases the resting transmembrane potential (TMP) of cells in the targeted region. The induced increase of this transmembrane potential is dependent upon various pulse parameters including applied voltage, electrode spacing, electrode insertion depth, number of pulses, pulse duration, and repetition rate. When performed using low energy pulses, the electroporation is considered reversible, which allows drugs, DNA, and other exogenous agents that otherwise would not be membrane permeable to be transported inside the cell for various treatments and applications. If performed above a certain threshold, utilizing high energy pulses, the permeabilization of the membrane becomes permanent in a process known as irreversible electroporation.

Irreversible electroporation (IRE) is a non-thermal ablation method to kill tumors utilizing pulsed electric fields that disrupt the plasma membrane of cancer cells to such a point that they cannot recover [5-7]. Irreversible electroporation involves the application of short duration, high intensity PEF to create defects in the plasma membrane, structurally changing the membrane leading to cell death. Irreversible electroporation offers benefits over other cancer therapies in that it can be performed near large blood vessels, nerves, and ducts without damage to these structures, sparing extracellular matrix. Thermal therapies cannot be performed near large blood vessels or other critical structures as blood flow carries heat away from the region of interest (heat sink effect), not allowing high critical temperatures to be reached in order to kill diseased

tissue. In addition, IRE is minimally invasive and allows for sub-millimeter resolution between treated and un-treated tissue, as well as visualization using real-time imaging, allowing the surgeon immediate confirmation of treatment [7, 8].

The mechanism by which these defects are created and remain permanent is still a subject of debate. The aqueous pore hypothesis is one of the main theories describing this phenomenon and will be discussed in the following sections, as well as the theory behind electroporation.

2.2 Theory of Electroporation

2.2.1 Background

Understanding the cell physiology and theory behind electroporation is important for further development of the technology. Electroporation in biological cells involves a rearrangement of the structure of the cell membrane [9]. The cell membrane of biological cells acts as a protective and regulatory barrier consisting of a lipid bilayer of hydrophilic heads and hydrophobic tails. The membrane is permeable to water, oxygen, carbon dioxide, and some hydrophobic molecules but impermeable to hydrophilic molecules. Molecules are transported across this membrane by various processes including endocytosis, facilitated diffusion, and active transport. Maintenance of Na^+, K^+, Ca^{2+}, and Cl^- ion gradients is essential for cell viability. Electroporation increases cell permeability, disrupting the diffusion of ions across the plasma membrane, as well as increasing the transmembrane potential which scales with membrane permeability [10].

2.2.2 Effect of the Electric Field on Cells

The cell membrane is considered to be a thin, insulative sheet surrounded by a conductive solution consisting of the extracellular matrix [11]. When a high electric field is applied to the cell, the conductivity increases resulting in an increase in the transmembrane potential of the cell, leading to electrical breakdown [12]. This induced transmembrane potential will result in cell membrane permeabilization, disrupting ionic gradients leading to reduction in the Na^+ and K^+ gradients with a large influx of calcium ions [11]. This electrical breakdown and facilitation of uncontrolled ion gradients is generally attributed to the creation of aqueous pores in the lipid bilayer as can be seen in Figure 1 [12, 13]. The transient aqueous pore theory is one of the main theories describing the mechanism behind electroporation.

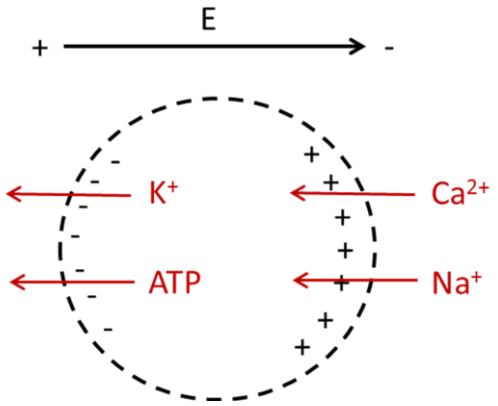

Figure 1: Polarized cell in an electric field showing membrane permeabilization and disruption of ion gradients

2.2.3 Transient Aqueous Pore Theory

While the molecular mechanism by which electroporation takes place is subject to debate, the transient aqueous pore theory is considered by many to be one of the main theories behind the electrical breakdown of the cell membrane after the application of pulsed electric fields. The theory hypothesizes that when an electrical field is applied to a cell membrane, there is a restructuring of this lipid bilayer of the membrane as aqueous pores are created, allowing foreign molecules to enter the cell. In reversible cases the pores reseal themselves, but for higher conductivities the cell ruptures [14]. Initially, thermal fluctuations result in hydrophobic pores which are essentially gaps in the lipid bilayer of the membrane as can be seen in Figure 2. However, as the pores reach a critical radius it becomes energetically favorable for them to

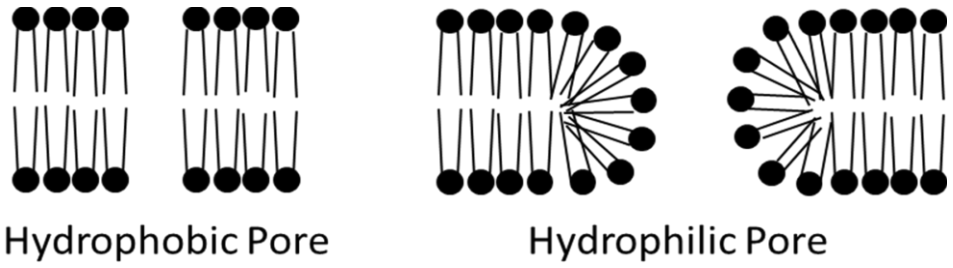

Figure 2: Hydrophobic (non-conducting) pores in the lipid bilayer and hydrophilic (conducting) pores.

transition to hydrophilic pores (Figure 2), which allow the passage of water-soluble molecules after becoming meta-stable [12].

The electroporation process is based off of the Smoluchowski equation which describes pore distribution as a function of their radius and time. Pores of radius, *r*, will expand and contract to minimize the pore energy function listed below [9]:

$$E(r) = 2\pi\gamma r - \pi\Gamma_0 + \left(C/r\right)^4 - \left\{\left(\epsilon_w - \epsilon_m\right)/(2h)\right\}\pi r^2 V^2 \quad (1)$$

where γ is the energy per unit length of the pore perimeter, Γ_0 is the energy per unit area of the membrane, h is the membrane thickness, V is the voltage across the membrane, and ϵ_w and ϵ_m are the permittivities of water and the lipid bilayer. As previously stated, hydrophobic or non-conducting pores are created first and the energy, $u(r)$, for these pores is described by:

$$u(r) = E_* \left(\frac{r}{r_*}\right)^2 \quad (2)$$

As $r > r_*$, approaches a critical radius it spontaneously changes to form an inverted conducting (hydrophilic) pore as it is now more energetically favorable to do so as can be seen in Figure 3 [12].

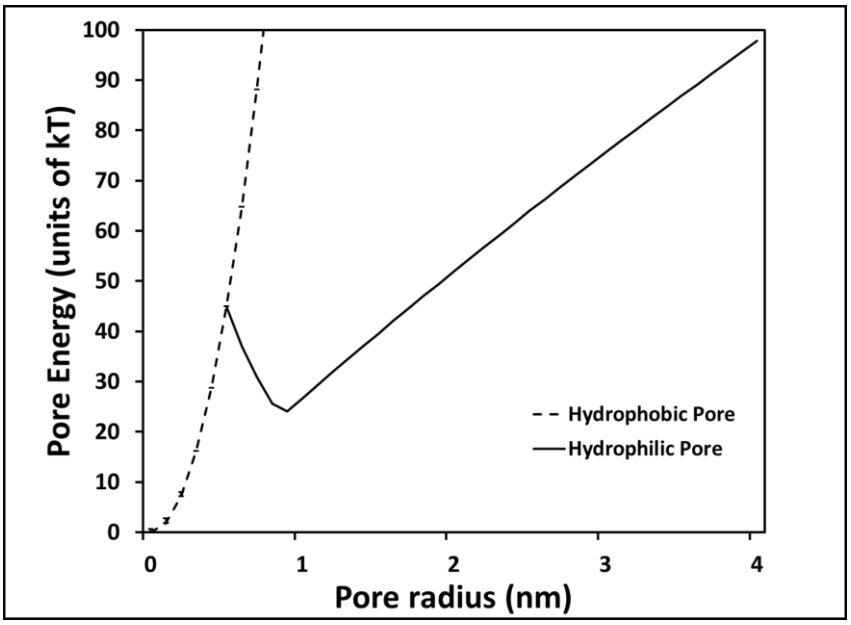

Figure 3: Pore formation energy for hydrophobic and hydrophilic pores. Figure generated with values from Neu et al [12].

The energy, *w(r),* for a hydrophilic pore is described by the first term of the Smoluchowski equation [12]:

$$w(r) = 2\pi\gamma r - \pi\sigma r^2 + \left(\frac{C}{r}\right)^4 \quad (3)$$

where γ is the energy per unit length of the pore perimeter, and $\Gamma_0 = \sigma r^2$ from Eq. 1 . The third term, added by Krassowska et al., represents steric repulsion where *C* is a constant and describes an increase in pore energy with shrinking radius.

The equation initially corresponds to the pore energy with no induced transmembrane potential and a stable radius of 0.8nm as can be seen in Figure 3. However, with electroporation, as voltage is applied there is an increase in the transmembrane potential and the last term in the Smoluchowski equation describes this:

$$\varphi(r,t) = w(r) - \pi a_p V^2 r^2 \quad (4)$$

The second term is the capacitive contribution in which $a_p = ((\epsilon_w - \epsilon_m)/(2h))$, and describes the membrane and aqueous properties of the pore [12]. Irreversible electroporation occurs when the transmembrane potential exceeds a certain threshold *(V=1.0V),* leading to pore expansion and irreversible breakdown of the lipid bilayer.

2.2.4 Transmembrane Potential of Electroporated Cells

Exposure of a cell to an electric field leads to an induced transmembrane potential, $\Delta\Psi_{m,}$ which is superimposed on to the natural resting transmembrane potential of the cell, and exists only as long as the external electric field is applied. The transmembrane potential can be derived from the following equation from Kotnik and Pucihar et al. [15]

$$\nabla\left(\left(\sigma+\varepsilon\frac{\partial}{\partial t}\right)\nabla\Psi(x,y,z,t)\right)=0 \quad (5)$$

which describes the spatial and temporal distributions of the electric potential. The time derivatives go to zero under steady-state conditions and the conductivity is assumed to be constant for the hydrogel model; therefore, the equation simplifies to Laplace's equation.

$$\nabla\cdot\nabla\Psi(x,y,z)=0 \quad (6)$$

In tissue and animal models, the conductivity term remains in Laplace's equation which can be challenging to estimate as the change in conductivity is often not known. Due to the low cell seeding density in the hydrogels, there is no bulk conductivity change, and therefore, this term is eliminated with the electric field distribution as the only remaining unknown variable. This is a great advantage that allows the hydrogel model to estimate the electric field distribution that can then be translated into tissue or animal models to determine the change in conductivity of a given tissue.

Although biological cells are not perfect spheres, they are often modeled as spheres of uniform thickness. Therefore, Laplace's equation can be solved under steady-state conditions for a spherical cell, which is known as the Schwan equation,

$$\Delta\Psi_m=1.5ER\cos\theta \quad (7)$$

where E is the electric field, R is the cell radius, and θ is the angle measured from the center of the cell with respect to the direction of the field [16]. This transmembrane potential is typically not established until several microseconds after the application of the electric field, and therefore, the first-order Schwan equation describes the transient behavior of the transmembrane potential in the microseconds before the steady-state equation takes hold. The first order Schwan equation is given as

$$\Delta\Psi_m = 1.5ER\cos\theta\left(1 - e^{-t/\tau_m}\right) \quad (8)$$

where τ_m is the time constant of the membrane charging,

$$\tau_m = \frac{R\varepsilon_m}{2d\frac{\sigma_i\sigma_e}{\sigma_i+2\sigma_e}+R\sigma_m} \quad (9)$$

and σ_i, σ_e, and σ_m are conductivities of the cytoplasm, extracellular matrix, and cell membrane, respectively, and ε_m is the dielectric permittivity of the membrane, d is the membrane thickness, and R is the cell radius.

2.2.5 Analytical Solution of the Electric Field Distribution

Irreversible electroporation requires that the local electric field be above a certain threshold which is greater than the reversible threshold, in order to cause permanent damage to the cell membrane leading to cell death. While many parameters affect the outcome of pulsed electric fields in treating cells, the magnitude of the local electric field within the target tissue is one of the most important. Numerical modeling is generally used to estimate this local electric field or conversely to determine an electrode setup based on a target electric field. Additionally, numerical modeling is also used to estimate the electric field distribution for complex needle geometries. For simplified 2D geometries, the electric field distribution can be estimated by solving Laplace's equation analytically.

Here Laplace's equation is solved analytically for a simplified 2-D, two needle electrode setup as shown in Figure 4 . Laplace's equation can be considered a two-dimensional problem if the needles are assumed to be long, of uniform thickness, and fully inserted into the tissue in which the needle penetration depth is larger than the distance between the electrodes.

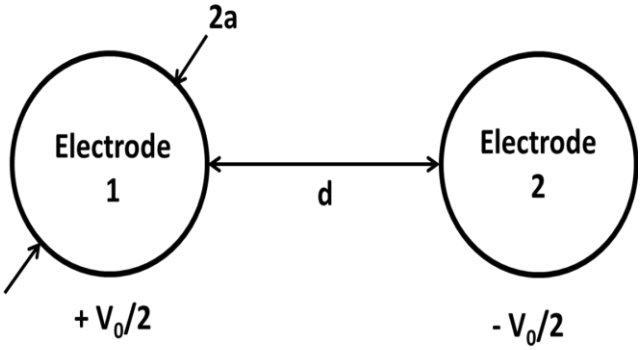

Figure 4: 2 Needle electrode setup for solving the analytical solution

The needles are represented as circles of radius, *a* with a distance, *d* between them and the tissue is assumed to be at a constant conductivity so that the potential of the needles is determined by solving Laplace's equation:

$$\nabla^2\varphi(z) = 0 \qquad (10)$$

where φ is the electric potential. This is a complex analytic function whose real part satisfies Laplace's equation where $z = x+iy$. The equation can be rewritten as the sum of potentials generated by each needle based on superposition:

$$\varphi(z) = \sum_{n=1}^{N} \varphi_n(z) \qquad (11)$$

where N equals the number of electrodes (N=2 in this case) and $\varphi_n(z)$ can be written as a sum of the leading terms of all n electrodes, neglecting higher multipole terms based on the leading order approximation as described in [17, 18].

$$\varphi_n(z) = \sum_{n=1}^{N} C_n \log\left(\frac{a}{z - z_n}\right) + C_0 \qquad (12)$$

For N=2 electrodes, Eq. 12 is expanded and constants $C=C_1= -C_2$:

$$\varphi(z) = Clog\left(\frac{z - z_2}{z - z_1}\right) \quad (13)$$

The gradient of the potential is taken with the derivative of a log as $\frac{d\log x}{dx} = \frac{1}{x\ln 10}$, resulting in the electric field distribution given by

$$E(z) = \frac{d\varphi(z)}{dz} = \frac{C}{ln(10)} * \left[\frac{1}{(z - z_2)} - \frac{1}{(z - z_1)}\right] \quad (14)$$

The constant, *C*, can then be found by applying the boundary conditions to Eq. 13 with respect to needle two. The potential, $\varphi = -V_0/2$ when $z\text{-}z_1 = z_{12} + ae^{i\theta} = z_{12} = d$, and $z\text{-}z_2 = ae^{i\theta} = a$ using Euler's formula $(e^{i\theta} = cos\theta + isin\theta)$ where $\theta = 0$ (Figure 5).

$$C = \frac{V_0}{2\log\left(\frac{d}{a}\right)} \quad (15)$$

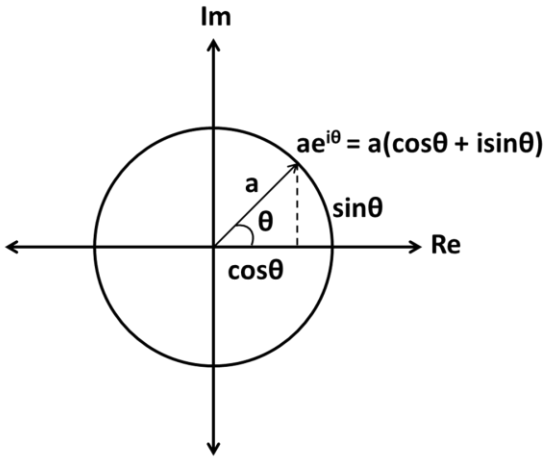

Figure 5: Euler's formula: sine and cosine functions are the real (Re) and imaginary (Im) parts of the complex exponential function given by Euler's formula.

The electric field can be obtained by plugging this constant, *C*, into Eq. 14, resulting in the final equation to estimate the electric field based on needle electrode parameters and applied voltage.

$$E(z) = \frac{V_0}{2 * \ln(10) * log\left(\frac{d}{a}\right)} * \left[\frac{1}{a} - \frac{1}{d}\right] \quad (16)$$

The estimated electric field for 300V applied at the center of the hydrogel is 1372 V/cm, for 375V applied is 1715 V/cm, and for 450V applied is 2058 V/cm. These values are close to the electric fields determined in numerical modeling indicating that the electric field distribution used to determine thresholds is correct.

2.2.6 Numerical Modeling of the Electric Field Distribution

Calculations of the electric field threshold required for cell death were determined using finite element analysis (COMSOL Multiphysics 4.2a, Stockholm, Sweden). The model reconstructed the 3-D geometry of the hydrogel and electrode setup, and the electric field (Figure 6) was

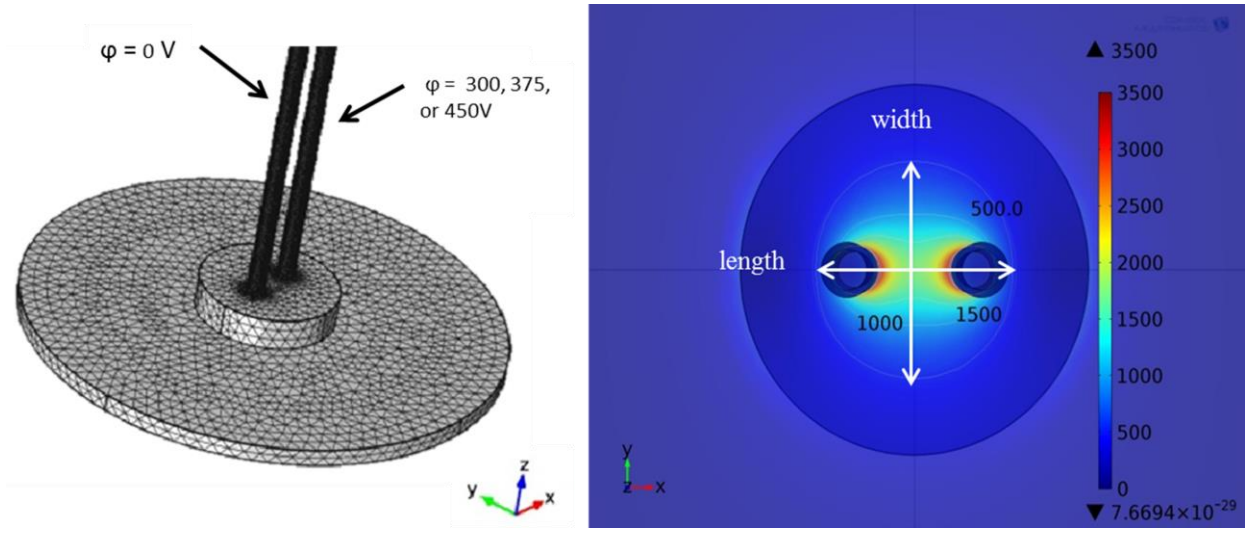

Figure 6: 3D reconstruction of hydrogel setup with boundary conditions in Comsol on the left. Electric field distribution (V/cm) for 450V applied denoting length and width measurements on the right.

calculated at points from the center to the edge along the hydrogel. The hydrogel consists of a large cylinder representing the well plate with a radius of 1.7 cm with the hydrogel sitting in the

center at *x=y=z=0*. The hydrogel is 10 mm in diameter and 2.25 mm in height. Two needles electrodes of infinite length and a diameter of 1.3 mm are inserted in the center of the hydrogel with a center-to-center spacing of 3.35 mm. Material properties are applied to all components by assigning electrical conductivity and relative permittivity values for the hydrogel, well plate, and needle electrodes. The well plate has an electrical conductivity of 1e-16 S/m, while the electrodes are made of stainless steel and have an electrical conductivity of 2.22e-6 S/m, and the hydrogel has an electrical conductivity of 1.2 S/m. The relative permittivity for all three materials is set to zero. Boundary conditions were set to specify electric potentials in which one electrode is electrically insulating with $\varphi = 0V$, while the other is electrically conductive with $\varphi = V_0$. The remainder of the boundaries in the model, including the hydrogel and well plate are set as insulation. An extremely fine user controlled mesh was used resulting in a <0.01% difference in electric field calculations with successive refinements. The electric field distribution is numerically solved from Laplace's Equation:

$$\nabla^2\varphi(z) = 0 \qquad (17)$$

where φ is the electric potential. A parametric study on voltage was performed to determine the electric fields along points across the hydrogel for 300V, 375V, and 450V. A line graph was drawn from the center of the hydrogel at *x=y=0* and *z= (height of the hydrogel/2)* which is directly in the center of the electrodes, and therefore, in the center of the electric field distribution (Figure 7).

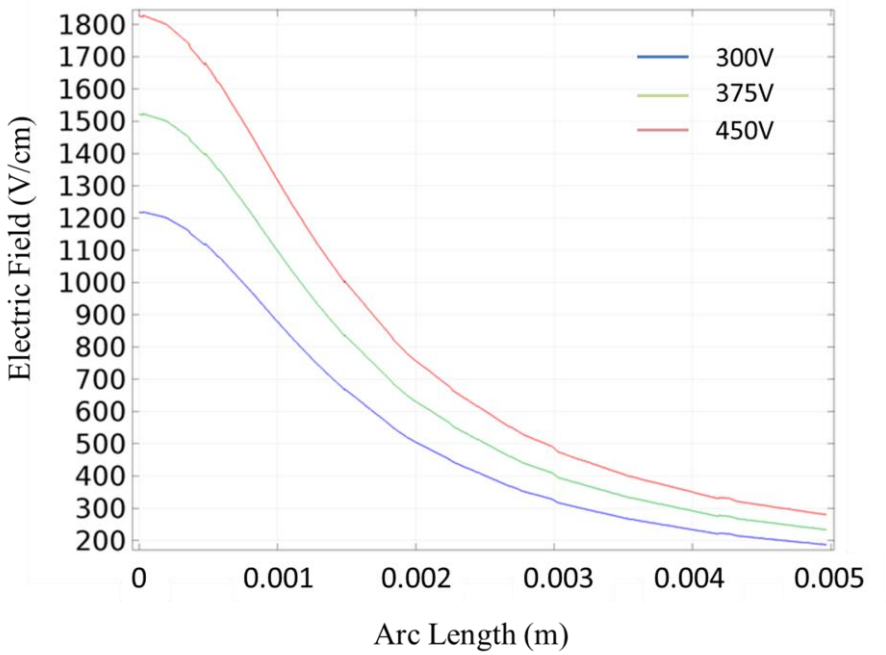

Figure 7: Electric field values from the center to the edge of the hydrogel along the width dimension for various applied voltages

Electric field values for the three applied voltages were solved at points along the line. Experimental width measurements of the lesion area were then correlated with the numerical model to determine the electric field thresholds for cell death at the transition between live and dead cells as previously described in Arena et al [19].

2.3 *In vivo* Studies of Irreversible Electroporation

The history of electroporation dates back to the 1970s during which time the dielectric breakdown of the plasma membrane due to an induced electric field was first discovered. In 1967, Hamilton and Sale discovered the effect of high electric fields on microorganisms when they delivered high electric pulses to bacterial cells, and noted the death of the cells was not due to thermal effects, but rather to the strength of the applied electric field [20]. Other studies around that time investigated the voltage necessary to achieve electrical breakdown of the cell membrane of various cells. Crowley et al. determined that the critical voltage may depend on

membrane properties through experiments with cholesterol, while Zimmermann et al. suggested that membrane properties as well as the shape factor of cells plays a role in the critical voltage necessary for electrical breakdown through his studies with red blood cells [21, 22]. The effects of pulsed electric fields on cells were further investigated by Neumann et al., who found that treatment of chromaffin cells with electric pulses resulted in permeabilization and calcium release from the cell [23]. While there have been many *in vitro* studies on electroporation in general, the molecular mechanism behind the electroporation is still ambiguous. Furthermore, reversible electroporation had been investigated for cancer treatment as well as for food and water sterilization before irreversible electroporation became a desirable therapy as well [5].

There have been many *in vitro* studies of irreversible electroporation, however, few studies have looked into the electric field threshold for cell death of different tissues. From the literature, the electric field threshold for cell death has only been documented *in vivo* for liver tissue, brain tissue, and for orthotopic mammary tumors in mice [24-28]. Miklavcic et al. documented an electric field threshold for cell death of 637 ± 43 V/cm for liver tissue through their i*n vivo* experiments with rabbits [24, 25]. This threshold was determined based on 8 pulses at 450V for 100 μs using needle electrodes with varying diameters. The study was focused on determining the thresholds for both irreversible and reversible electroporation, in order to optimize DNA electrotransfer for gene therapy above the reversible electroporation threshold but below the irreversible threshold. The reversible threshold for *in vivo* rabbit liver was found to be 362 ± 21 V/cm. The irreversible threshold was determined by incrementally increasing voltage to liver samples until necrosis was evident, at which point this voltage was considered the threshold voltage for irreversible electroporation. The corresponding electric field threshold for cell death

was then determined [25]. Edd et al. performed a similar i*n vivo* experiment in rat liver using 10 mm diameter, 1 mm thick plate electrodes with a 4 mm gap between electrodes, pulsed at 400V for one, 20 ms long pulse. It was determined that the transition from reversible electroporation to irreversible occurred between 300 and 500 V/cm with electric field strengths consistently between 900 and 1100 V/cm [24]. A third study on perfused porcine livers demonstrated an electric field threshold of 423 ± 147 V/cm. The study used *ex vivo*, perfused porcine livers within 24 hours of animal sacrifice to determine whether electroporation can be used as a means to decellularize tissue scaffolds. Livers were treated using two metal plate electrodes with a 2 cm diameter with 99, 100 μs pulses delivered at varying repetition rates. The threshold in this study was found to be lower than the previous which could be due to specific pulse parameters or due to the perfusion environment [26].

The electric field threshold for brain tissue has also been documented in the literature by Garcia et al. The study was performed in canine subjects using 1 mm diameter needle electrodes pulsed with nine sets of ten pulses at 4 Hz with 1000V and 500V applied. Through correlation with numerical models, the electric field threshold for cell death of i*n vivo* brain tissue was found to be 495-510 V/cm [27].

Lastly, the electric field threshold has been determined for orthotopic mammary tumors grown in mice. Treatment used a bipolar needle electrode administering 100 pulses of 100 μs pulse length, while reversing polarities every 25 pulses with an applied voltage of 1300 V/cm. The electric field threshold for cell death in these tumors was 1000 V/cm which was consistent with *in vitro* studies [28].

From the *in vivo* studies presented here, it can be seen that the electric field threshold for irreversible electroporation to occur can be considered to be above 500 V/cm, although this may depend on tissue type. It was noted that liver models determined thresholds for irreversible electroporation ranging from 423 to 637 V/cm while brain required ~500V/cm and orthotopic mammary tumors in mice exhibited a higher 1000 V/cm threshold. Therefore, it is necessary to investigate the thresholds of other cancer cell types in order to further develop the technology, improve treatment planning models, and increase the acceptance of irreversible electroporation as a primary cancer therapy. Based on the few threshold values presented in literature, it is expected that the thresholds for pancreatic and prostate cancer would fall within a similar range. Particularly between 500 and 600 V/cm, as this is the threshold seen most often; however, values as low as 400 V/cm or as high as 1000 V/cm could also be seen due to varying tissues, experimental effects, or specific pulse parameters.

2.4 Clinical Studies of Irreversible Electroporation

While the IRE technology is still developing, there have been some beginning phase clinical trials performed on prostate, pancreatic, kidney, liver, and lung cancer. One of the first clinical trials was performed at Alfred Hospital in Prahran, Victoria, Australia. The objective of this study was to determine the short-term safety and to test the IRE procedure in the clinical setting as anesthesia, muscle contraction, and arrhythmia problems were thought to present challenges. Twenty-one patients with 28 total procedures were treated involving eight kidney procedures, 17 liver, and three for the lung. Patients were under anesthesia and treated with two types of electrodes, bipolar and unipolar. For those treated with the bipolar needle, pulses were administered in groups of 10 with 70 μs pulse lengths while those treated with two or more

unipolar needles were pulsed in groups of 10 for 100 μs pulse lengths. Each treatment consisted of 90 pulses with voltages ranging from 500V- 3000V. Treatment was aborted if current peaked above 48 A, as thermal heating of the tissue can occur at higher current values. Additionally, needle placement was done under ultrasound or CT guidance. During IRE treatment, skeletal and diaphragm muscle stimulation occurred, requiring the administration of muscle paralytics. This was an anticipated challenge as muscle stimulation had been seen in *in vivo* studies previously. Another anticipated challenge dealt with during the treatment was heart arrhythmias as the large current IRE produces had been known to cause arrhythmias in pigs, treated with the therapy when needles were placed in close proximity to the heart. Of the eight renal patients, one experienced arrhythmia, while two of the three lung patients, and four of the 17 liver patients experienced some sort of arrhythmia during the procedure, despite some efforts to synchronize IRE pulse delivery with heart beats [29]. This study established irreversible electroporation as a viable therapy to treat tumors. As IRE was in the developmental stages, improvements were made for later clinical trials.

A second clinical safety study for irreversible electroporation was performed at Alfred Hospital in Australia on thirty-eight patients with advanced stages of liver, kidney, and lung cancers, totaling 69 tumors. Similar to the previous study, patients in this study were under general anesthesia with muscle relaxants, and either bipolar, or two or more unipolar electrodes delivered IRE pulses at the same parameters described in the first study. Of the liver tumors, 15 of 18 achieved complete target ablation three months post-IRE. Of the 7 kidney patients, 5 patients had complete tumors ablated at three months while the three patients treated with lung cancer did not have complete ablation as the tumors were not completely treated. This study proved that

IRE has advantages over thermal ablation techniques as it spared vasculature and bile ducts. In addition, synchronization of IRE pulsing with heart beats was a success and there were minimal complications [30]. As this was performed mainly as a safety study, further clinical trials need to be performed for various cancers to advance this treatment.

There have been additional studies into the use of irreversible electroporation on liver tumors, one by Dr. Kingham in New York and another by Dr. Cannon and Dr. Martin in Kentucky. In the former study, tumors were primarily chosen in patients to be <2cm from large hepatic veins or portal pedicles in order to prove the efficacy and safety of IRE near critical structures. The IRE procedure was performed as previously described in other clinical studies in which 90 pulses were delivered. A total of 28 patients were treated over a 10 month period with 65 tumors being treated in 31 total procedures. From this study there were six local recurrences of tumors when analyzed six months post-IRE with the average ablation area being 9 cm^2, one month post-IRE. Overall, IRE's ability to treat perivascular tumors shows great potential for it to become a primary cancer therapy for unresectable tumors [31]. The latter study by Dr. Cannon and Dr. Martin also focused on the safety and efficacy of IRE to treat hepatic tumors near vital structures. This was a prospective study over two years in which tumor characteristics and treatment outcomes were analyzed, as well as the local recurrence free survival for ablated lesions based on Kaplan-Meier. Similar pulse parameters as previously described were used in this study on 44 patients with a total of 48 IRE procedures. The local free recurrence at 3, 6, and 12 months was 97.4%, 94.6%, and 59.5%, respectively. However, smaller tumors experienced less recurrence with local free recurrence rates at 3, 6, and 12 months of lesions <3cm were 100%, 100%, and 98% [32]. This study further proves the efficacy and safety of IRE for the

treatment of unresectable tumors even those located near vital structures. It can be seen from these trials that larger tumors are harder to ablate and that those <3cm in size had the best outcomes.

Furthermore, irreversible electroporation as a therapy for pancreatic and prostate cancer have also been investigated in human clinical trials. IRE's efficacy in treating pancreatic cancer was assessed in a 76 year old male with stage II, unresectable pancreatic adenocarcinoma. The tumor was 4.1 x 4.1 x 3.5 cm, encasing the celiac axis and superior mesenteric artery. The previous studies investigated IRE's ability to treat perivascular hepatic tumors, and therefore, treating perivascular tumors in other tissues needed to be investigated. Four needle electrodes were used to treat the tumor in two IRE procedures with 90 pulses as previously described in clinical liver trials. The procedure was aborted at pulse 70 due to current exceeding 50 A. A second IRE procedure was performed 2 weeks later. Three months post-IRE there was no residual tumor evident; however, a liver metastasis did occur [33]. IRE shows great promise for treating pancreatic cancer especially as the anatomy limits the resection and the effectiveness of thermal therapies, however, optimal treatment planning methods still need to be investigated.

Similar to pancreatic cancer, prostate cancer anatomy often limits thermal therapy effectiveness with resection often not being an option. IRE as a potential therapy to treat this cancer has been investigated with the first clinical trial in 2010. Four needle electrodes were placed in a pattern surrounding the tumor with electrode pairs being energized at different times until all permutations were covered. The pulsing protocol was similar to other clinical trials with 90 pulses being applied with 70-100 μs pulse lengths with a 100 ms interval between pulses at an

applied voltage of 1500V. Of the 16 patients, 15 had no evidence of cancer in postoperative biopsies and vital structures remained intact and functioning [34].

Beginning phase clinical trials for irreversible electroporation have shown its safety and efficacy in treating lung, kidney, liver, pancreatic, and prostate cancer including tumors near vital structures. The beginning clinical trials have also shown promising results for the continued use of this technology in the treatment of cancer. Further understanding of the technology, particularly of varying pulse parameters and improving treatment planning models are necessary. Understanding the thresholds necessary to kill different cancers as well as varying pulse parameters and electrode geometries will help to improve and optimize treatment planning models for patients.

Chapter Three: Methods

3.1 Cell Culture

Grade IV human prostate adenocarcinoma cells (PC 3) derived from bone metastasis, and human prostate carcinoma cells (DU-145) derived from brain metastasis were purchased from ATCC (ATCC, Manassas, VA). The PC-3 cells were cultured in F-12K (Kaighn's) Medium, a modification of Ham's F-12 Growth Medium, supplemented with 10% fetal bovine serum (Sigma Aldrich, St. Louis, MO)/1% penicillin streptomycin (Invitrogen, Carlsbad, CA) and grown to 75% confluency for prostate cell characterization experiments. The DU-145 cells were grown in RPMI 1640 with L-glutamine and supplemented with 10% fetal bovine serum (Sigma Aldrich, St. Louis, MO)/1% penicillin streptomycin (Invitrogen, Carlsbad, CA) and were also grown to 75% confluency for prostate cell characterization experiments. Pancreatic cancer cell characterization experiments were implemented using PANC-1 and BxPC-3 cell lines. PANC-1 is a human pancreatic cancer derived from a primary ductal epithelioid carcinoma, purchased from ATCC (ATCC, Manassas, VA) and cultured in Dulbecco's Modified Eagle's Medium supplemented with 10% fetal bovine serum (Sigma Aldrich, St. Louis, MO)/1% penicillin streptomycin (Invitrogen, Carlsbad, CA). BxPC-3 is a pancreatic adenocarcinoma derived from a primary tumor and was cultured in RMPI 1640 Medium supplemented with 10% fetal bovine serum (Sigma Aldrich, St. Louis, MO)/1% penicillin streptomycin (Invitrogen, Carlsbad, CA). Both pancreatic cancer cell lines were grown to 75% confluency to be used for pancreatic cell characterization experiments.

3.2 Collagen I Hydrogel Extraction and Polymerization

Collagen I hydrogel extraction and formation of *in vitro* tumors were based off of previous protocols [19, 35] Rat tail tendons from Sprague Dawley rats were extracted and dissolved overnight in pH 2.0, 0.1M hydrochloric acid with agitation. The collagen I was centrifuged at 30,000 x g, 4°C for 45 minutes, the supernatant decanted and set volumes of 0.25mL, 0.5mL, and 1.0mL removed for concentration determination. Weighed volumes were dried in an oven at 75°C overnight in order to remove all HCl from the collagen. Samples were then re-weighed the following day to determine the collagen concentration. The collagen was sterilized by layering over chloroform overnight, and the final collagen batch pipetted off the chloroform the following day. Collagen was then stored at 4°C until ready for use. Collagen was made every two weeks or as needed.

In order to maintain cell viability in the hydrogel, a neutralizing buffer consisting of 10X DMEM, 1N NaOH, and dH_2O was used to re-suspend a cell pellet at a final cell seeding density of $5x10^6$ cells/ml. Cells were passaged according to ATCC cell protocols and 1mL of cells placed in the Vi-Cell to determine cell viability.

The total volume of hydrogel solution needed to make the desired number of hydrogels was chosen and used in calculations to determine the appropriate volumes of neutralizing buffer and collagen. The volume of collagen was always at a concentration of 8 mg/mL, and was determined by the total volume of hydrogel solution and the initial concentration of the collagen batch being used to make hydrogels.

$$V_1 = Total\ Volume\ of\ Hydrogel\ Solution \quad (18)$$

$$V_2 = Volume\ of collagen = \frac{V_1 * 8mg/mL}{Initial\ Collagen\ Concentration} \quad (19)$$

As previously stated, the neutralizing buffer consisted of 10X DMEM, 1N NaOH, and dH_2O. The volumes of these components were calculated as follows:

$$V_3 = Volume\ of\ 10X\ DMEM = \frac{V_1}{10} \quad (20)$$

$$V_4 = Volume\ of\ 1N\ NaOH = V_2 * 0.02 \quad (21)$$

$$V_5 = Volume\ of\ dH_2O = V_1 - (V_2 + V_3 + V_4) \quad (22)$$

The neutralizing buffer was mixed together without collagen, and the cell pellet resuspended in a pre-chilled sterile tube at a concentration of $5x10^6$ cells/mL and placed on ice. Collagen was then added to the neutralizing buffer/cell mixture, and mixed before immediately being pipetted into well plates. Six well plates were used to pipette 235 µL into 10 mm cylindrical PDMS molds as seen in Figure 8.

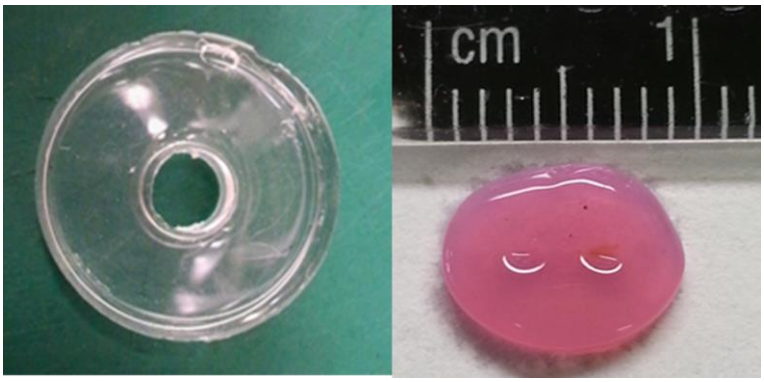

Figure 8: PDMS mold on the left with hydrogel on right.

After polymerization for 20 minutes at 37°C, molds were removed from the hydrogels and 2mL of media added to each well to maintain cell viability. Hydrogels were incubated overnight in media before IRE treatment the following day.

3.3 Hydrogel IRE Treatment

Media was aspirated from the wells containing hydrogels with hydrogels remaining in six well plates for IRE treatment. IRE pulses were delivered using 1.3 mm diameter stainless steel hollow needles with a 3.35 mm center-to-center spacing as seen in Figure 9.

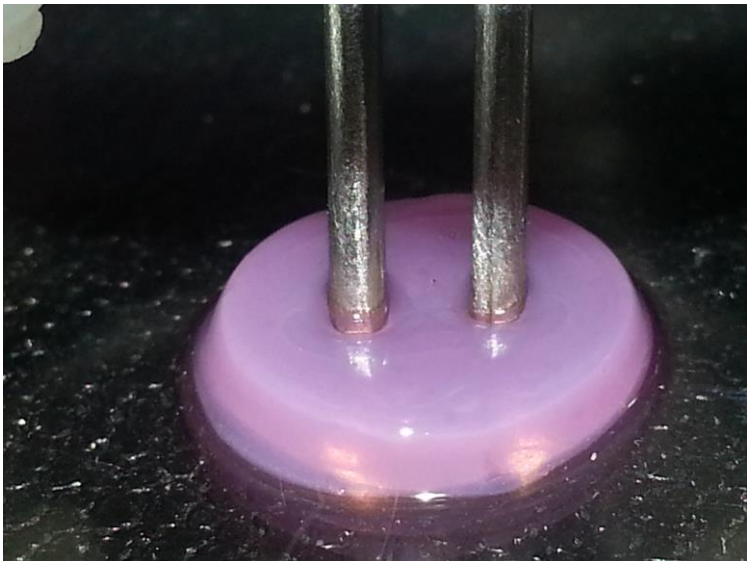

Figure 9: Hydrogel with stainless steel hollow electrodes inserted. Electrodes have a center-to-center distance of 3.35 mm and have a 1.3 mm diameter.

IRE pulses were delivered for 100 μs long pulses for a total of 80 pulses with a repetition rate of 1 pulse/second using an ECM 830 electroporation system (BTX-Harvard Apparatus, Holliston, MA) as can be seen in Figure 10. Pulses were applied for voltages of 300V, 375V, and 450V in order to achieve electric fields ranging from 1000-1500 V/cm, and pulse parameters were chosen based on existing IRE protocols [8, 19, 36]. Needle electrodes were inserted into the center of

Figure 10: Hydrogel experimental setup with 6 well plate, electrodes, and BTX.

hydrogels for pulse delivery and cleaned with ethanol in between each hydrogel. Electrodes were inserted into control hydrogels without pulsing in order to validate that any observed effects resulted from irreversible electroporation only. Post-treatment, media was added to the well plates and hydrogels were incubated from a range of 2 hours to 96 hours to eliminate effects due to reversible electroporation before post-IRE analysis.

3.4 Viability Analysis and Fluorescent Imaging

Post-IRE pulse delivery, hydrogels were incubated for 2, 24, and 48hrs, and 72 and 96 hrs, prior to viability assessment in order to eliminate any reversible electroporation effects as well as to determine the optimal time for analysis. Viability was assessed using a calcein acetomethoxy (AM)/propidium iodide (PI) live/dead assay. Calcein AM (4μM; λ_{em} = 515 nm; Invitrogen) was added at a concentration of 2 μl/ml to media 25 minutes prior to analysis, and propidium iodide

(1.5 mM; λ_{em} = 617 nm; Invitrogen) was added at a concentration of 30 µl/ml to media five minutes before analysis. Calcein AM stains live cells as it can be transported across the cell membrane, fluorescing green once intracellular esterases remove the AM group. Propidium iodide stains dead cells as it binds to nucleic acids emitting a red fluorescence. Staining was staggered five minutes between wells to insure that dye was added for the same amount of time to each sample prior to imaging.

Hydrogels were imaged using a Leica DMI 6000 fluorescent microscope (Leica Microsystems, Buffalo Grove, IL), tiling a set of images in order to reconstruct the entire hydrogel surface. Hydrogels were removed from the six well plate using forceps and placed upside down on a petri dish for imaging. A GFP filter was used to visualize the live cells while TXR was used to visualize the dead cells. Exposure, intensity, and gain were set for each filter to minimize saturation. Four points along the edges of the hydrogel were chosen in the tiling program in order to reconstruct the hydrogel surface. Live images and dead images were overlaid on top of each other to show the lesion volume, and measurements of the lesion dimensions were taken in the LAS software.

3.5 Confocal Imaging

In vitro tumor models are beneficial over typical *in vitro* cell suspension studies in that cells are able to attach to the hydrogel's matrix in which the cells are larger in size with morphologies similar to physiological environments. Actin and nuclei staining of the cells within the hydrogel were used to visualize the cells behavior with confocal imaging on a Zeiss LSM 510 Laser Scanning Microscope (Carl Zeiss Microscopy, LLC, United States). Hydrogels were washed twice with PBS for five minutes each and then fixed in 3.7% paraformaldehyde for 10 minutes.

Following fixation, hydrogels were rinsed three times for five minutes each prior to incubation for 25 minutes in a blocking and permeabilizing buffer, PBS-X consisting of PBS, Triton-X, and BSA. Rhodamine phalloidin (λ_{em} = 565 nm; Invitrogen) was used to stain for actin as it attaches to F-actin filaments and is conjugated with the fluorophore, eosin, for fluorescent visualization. DAPI (4',6-diamidino-2-phenylindole dihydrochloride; λ_{em} = 461 nm; Invitrogen) was used to stain for the nuclei as it binds to A-T regions of DNA. Both stains were dissolved in PBS-X, DAPI at 1:5000 ratio (0.2µl to 1ml PBS-X) and rhodamine phalloidin at 1:100 ratio (10µl to 1ml of PBS-X). Stains were added to hydrogels and let sit at room temperature for one hour, protected from light. Hydrogels were then rinsed three times for five minutes each with PBS and ready for imaging.

3.6 Scanning Electron Microscopy Imaging

Further understanding and visualization of the cell-to-cell interactions as well as the cell-to-matrix interactions were assessed using scanning electron microscopy (SEM). Scanning electron microscopy allows for high magnification images on the order of nanometers of the surface of a specimen. SEM scans electron beams producing images of the surface of a sample based on signals detected from the interactions of the sample's atoms with the electron beam. Samples are typically imaged in high vacuum SEMs, however, biological and wet samples can be imaged in a low vacuum, environmental SEM. There are various ways to prepare samples for SEM including freeze drying, chemical drying, or leaving biological samples wet. Samples that are nonconductive generally are coated with a thin layer of a conductive material such as gold palladium.

Field-emission scanning electron microscopy (FESEM) was used to look at collagen I hydrogels without cells while environmental scanning electron microscopy (ESEM) was used to look at hydrogels seeded with PC-3, PANC-1, DU-145, and BxPC-3 cells. Sample preparation for the two differed drastically as FESEM requires samples to be completely dry as it uses a high vacuum chamber, while ESEM can look at wet samples with lower vacuum pressures. For FESEM, collagen I hydrogels were frozen at -80°C for 24 hours to ensure the sample was completely frozen prior to freeze drying to eliminate cracking and structural damage to the sample. Samples were then freeze dried for 24 hours before FESEM sample preparation. Freeze drying or lyophilization is a dehydration process to preserve materials through the lowering of pressure in a vacuum to allow the frozen water in the sample to sublimate from the frozen, solid phase to the gaseous phase. After freeze drying samples were mounted using double-sided carbon tape and sputter-coated with a thin layer of gold palladium for 60 seconds. FESEM allowed for higher resolution images of the collagen matrix by using a LEO (Zeiss) 1550 field-emission scanning electron microscope (Carl Zeiss Microscopy, LLC, United States).

Biological or wet samples were imaged on a FEI Quanta 600 FEG (FEI Company, Hillsboro, OR) environmental scanning electron microscope. ESEM is performed at lower vacuum pressures and lower resolution, therefore allowing samples to remain hydrated without the need for freeze drying which would alter the structure of many biological samples. Hydrogels were seeded with PC-3, PANC-1, DU-145, and BxPC-3 cells. Hydrogels were cooled on a cold-stage and the temperature, pressure, and humidity within the chamber were adjusted to improve image resolution. Samples were first imaged at 100% humidity and slowly lowered to 60% humidity to

improve image resolution without completely drying the sample. Humidity can be lowered manually or as a result of choosing appropriate pressure and temperature values.

Chapter 4: Results

4.1 Overview

Two human prostate cancer and two human pancreatic cancer cell lines were treated with IRE and analyzed at various time points to determine the electric field threshold for cell death, as well as the amount of time post-IRE delivery for the lesion to become fully developed. The PC-3, PANC-1, DU-145, and BxPC-3 cell lines were run three times each. It was hypothesized that all four cell lines would have an electric field threshold between 500 and 600 V/cm based on the IRE thresholds found in literature for other cell lines [24, 37]. While the electric field thresholds for cell death have not been investigated for many cell lines, it was hypothesized that for two cell lines of the same cancer, the electric field threshold for cell death would be similar. Treatments for hydrogels were chosen randomly including the voltage to be applied to the hydrogel and the time points to analyze. For the first 2 trials of each cell line, 36 hydrogels were made with 12 hydrogels being analyzed at each time point of 2, 24, and 48 hours post-IRE. Three voltages, as previously described in methods, of 300V, 375V, and 450V were applied to hydrogels with each voltage being repeated three times per analysis time point in addition to control hydrogels. The total number of hydrogels was lowered for the third trial of experiments as only one control hydrogel, in addition to the nine (three for each voltage) treated hydrogels was found to be necessary. It should be noted that the second trial of DU-145 cells consisted of 2 additional analysis time points at 72 and 96 hours. Once lesion widths were determined at each time point, the lesion width dimensions were averaged for each voltage and this value used to determine the electric field threshold for cell death as previously described in numerical modeling. The electric

field thresholds for cell death were then averaged over all voltages and time points per cell line to determine the overall electric field threshold for cell death.

4.2 Prostate Cancer Cell Death Characterization in the Hydrogel Model

PC-3 and DU-145 were the two human prostate cancer cell lines used to determine the electric field threshold for cell death in the *in vitro* tumor model. The PC-3 cells exhibited consistent results supporting the hypothesized cell death threshold range. The DU-145 cells showed variable ranges for cell death slightly above the hypothesized range. Confocal imaging and scanning electron microscopy were used to further validate and understand the results. This section will further discuss the results from these two cell lines.

4.2.1 PC-3 Cell Death Characterization

The PC-3 cells had an electric field threshold for cell death ranging between 500 and 600 V/cm, comparable to thresholds shown in literature, which supported our hypothesis. The first trial of PC-3 cells resulted in an overall electric field threshold for cell death of 533 ± 7 V/cm. The electric field threshold remained similar between 2, 24, and 48 hour analysis time points. The lesion dimensions also remained similar between time points for the same voltage indicating that for PC-3 cells, analysis at all time points should be comparable. It was noted that lesion dimensions did increase with increasing voltage; however, they were consistent between time groups. Between voltages, the width dimensions grew from 3.89mm at 300V to 4.60mm at 375V to 5.54mm at 450V. At lower applied voltages, the electric field the hydrogels experienced was less, and therefore, the developed lesion was smaller. As the lesion dimensions remained similar between analysis times, the electric field remained consistent for the different

time groups indicating that this cell line can be imaged and the cell death threshold determined at any of the time points (Figure 11).

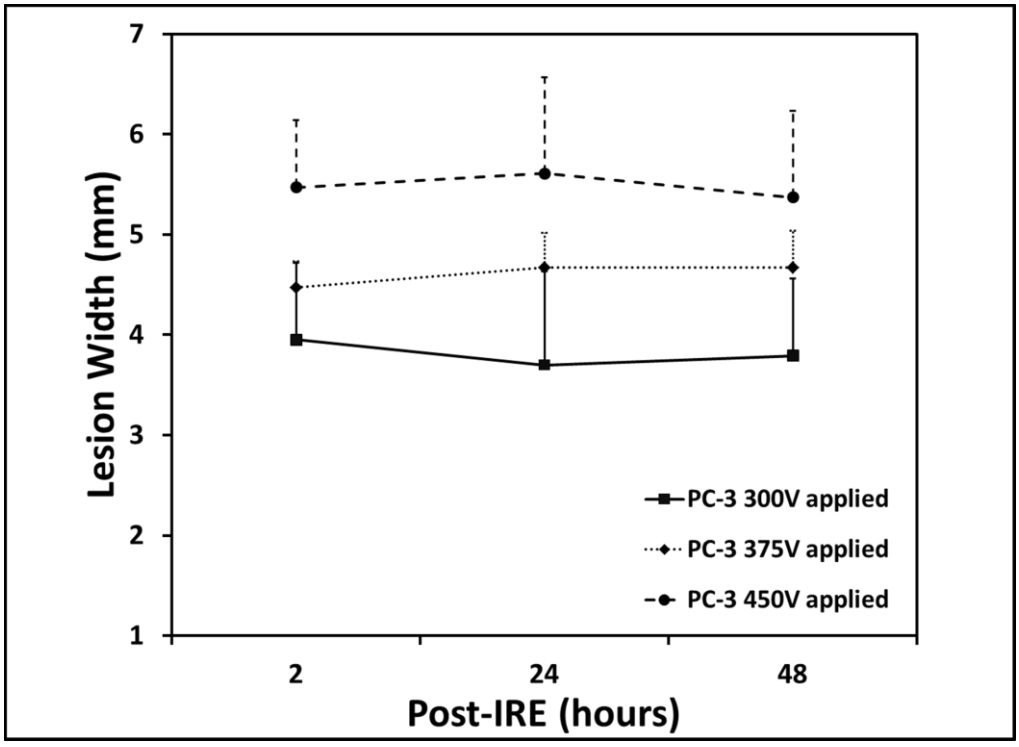

Figure 11: Lesion width vs time for PC-3 experiments showing lesion widths for each applied voltage

The second trial using PC-3 cells reaffirmed the results from the first trial. The electric field threshold for cell death of the PC-3 cells based on the second trial of experiments was 585 ± 6 V/cm. Similar to the first trial of experiments, the lesion dimensions remained similar between time groups with the width dimensions being the most variable, and; therefore, used to determine the electric field threshold for cell death. The averaged lesion widths across time points for varying voltage were as follows: 3.45 mm, 4.3 mm, and 5.18 mm at 300V, 375V, and 450V applied.

The third trial of PC-3 experiments resulted in an electric field threshold for cell death of 506 ± 10V/cm, remaining consistent and within the 500-600V/cm range with the first two trials. The lesion widths remained consistent between time groups and grew with increasing voltage as had been seen with the first two trials. The lesion widths at varying voltages averaged over three trials were 4.10 mm, 4.92 mm, and 5.73 mm for 300V, 375V, and 450V applied.

As the electric field threshold for cell death remained similar between trials as well as between

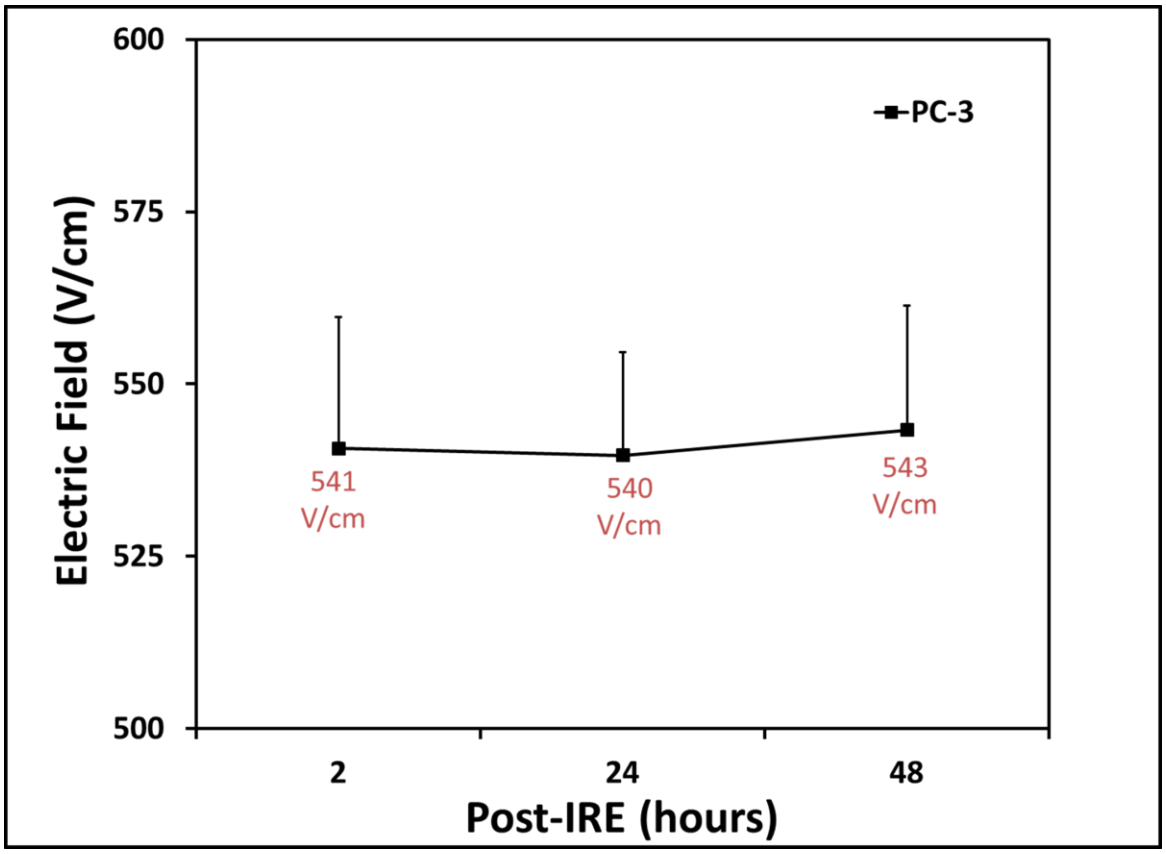

Figure 12: Electric field threshold for cell death for PC-3 experiments

time points post-IRE (Figure 12), the overall electric field threshold was taken as the average of the thresholds over all time points: 541 V/cm. Additionally, this threshold for PC-3 cells was validated through numerical modeling. The threshold estimated in the numerical model overlaid

on an image of the hydrogel stained with calcein AM and propidium iodide demonstrated a similar lesion as seen in Figure 13.

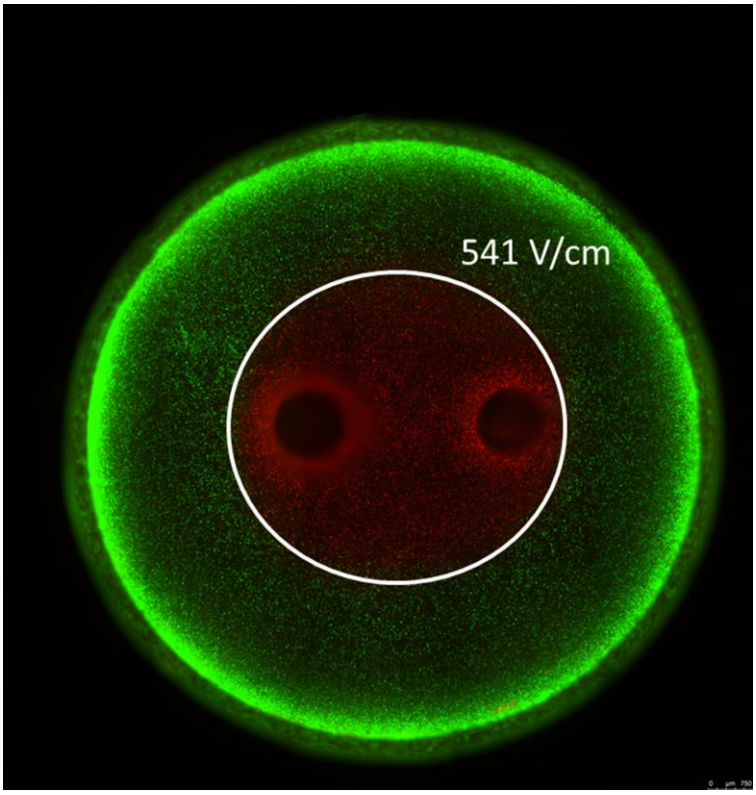

Figure 13: PC-3 electric field threshold for cell death overlaid on hydrogel

4.2.2 DU-145 Cell Death Characterization

The DU-145 cells showed more variability in results between trials with overall higher electric field thresholds for cell death above 600 V/cm. The first trial of DU-145 cells showed a higher than anticipated electric field threshold for cell death of 954 ± 124 V/cm, averaged over the 2, 24, and 48 hour time points. The lesion area was not fully developed by 48 hours, and therefore, this accounts for the high threshold for cell death as well as the high standard deviation. Figure 14 shows the lesion width over time for the DU-145 cell experiments. Due to the higher than hypothesized electric field threshold for cell death in the first trial, the second trial of DU-145

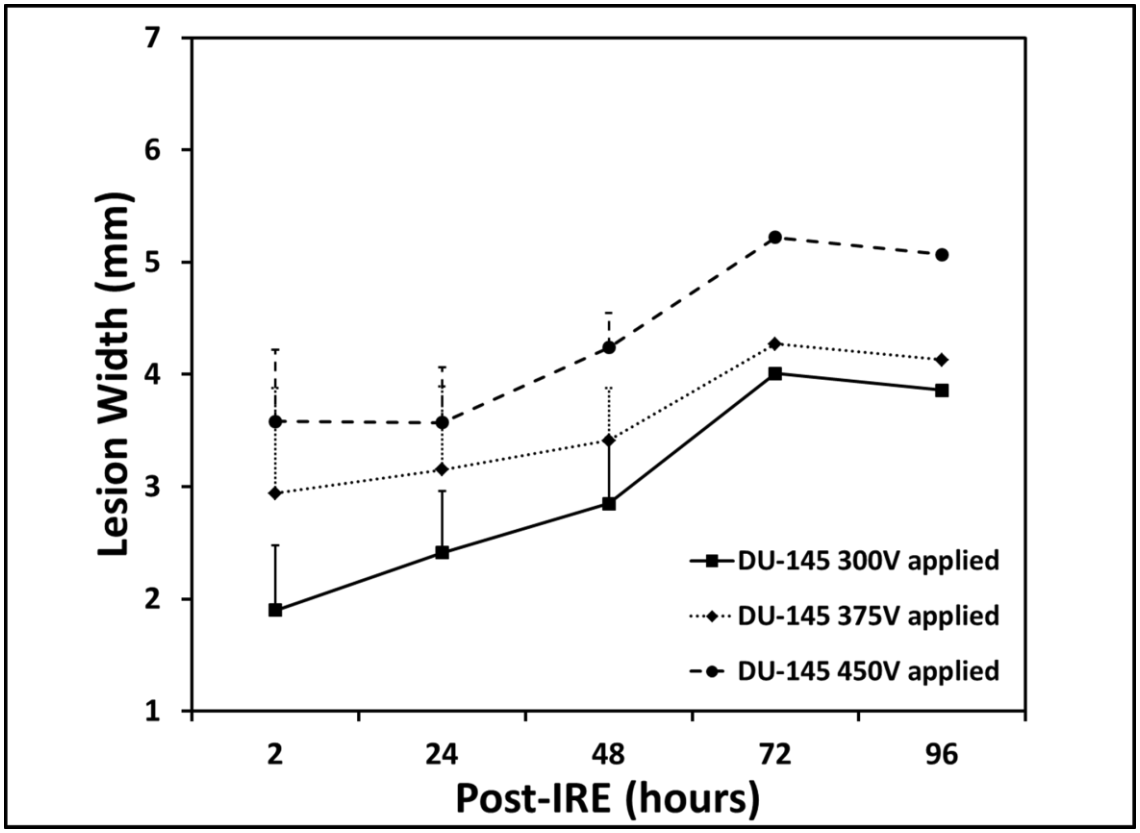

Figure 14: Lesion width vs time for DU-145 cells.

experiments included two additional analysis time points at 72 and 96 hours to determine whether the lesion needed more time to fully develop. The lesion was fully developed by the 72 hour time point; however, at 72 and 96 hours there were more cells dead within the entirety of the hydrogel including outside the lesion area. The lesion area was larger for higher applied voltages as was seen with the PC-3 cells with an average lesion width of 3.20 mm for 300V applied, 3.94 mm for 375V applied, and 4.51 mm for 450V applied in the first trial of DU-145 experiments. The electric field threshold for cell death of the second trial of DU-145 cells was 565 ± 17 V/cm and was taken as the average of the 72 and 96 hour time points. The second trial resulted in lower widths of 1.77 mm for 300V applied, 2.39 mm for 375V applied, and 3.25 mm for 450V.

A third trial of DU-145 cells was performed to better understand the variability in results between the first two trials as well as to determine whether the difference in lesion widths and corresponding electric fields could be due to experimental errors. During the third trial, DU-145 cells were analyzed at the same time points as the first trial of 2, 24, and 48 hours post-IRE pulse delivery. The overall electric field threshold for cell death for the third trial was taken as the threshold for the 48 hour analysis time point of 697 ± 12 V/cm. Similar to previous trials, the lesion widths grew with increasing voltage with a width of 2.67 mm for 300V applied, 3.35 mm for 375V applied, and 4.05 mm for 450V applied. The electric field thresholds for DU-145 cells at the chosen time points can be seen in Figure 15.

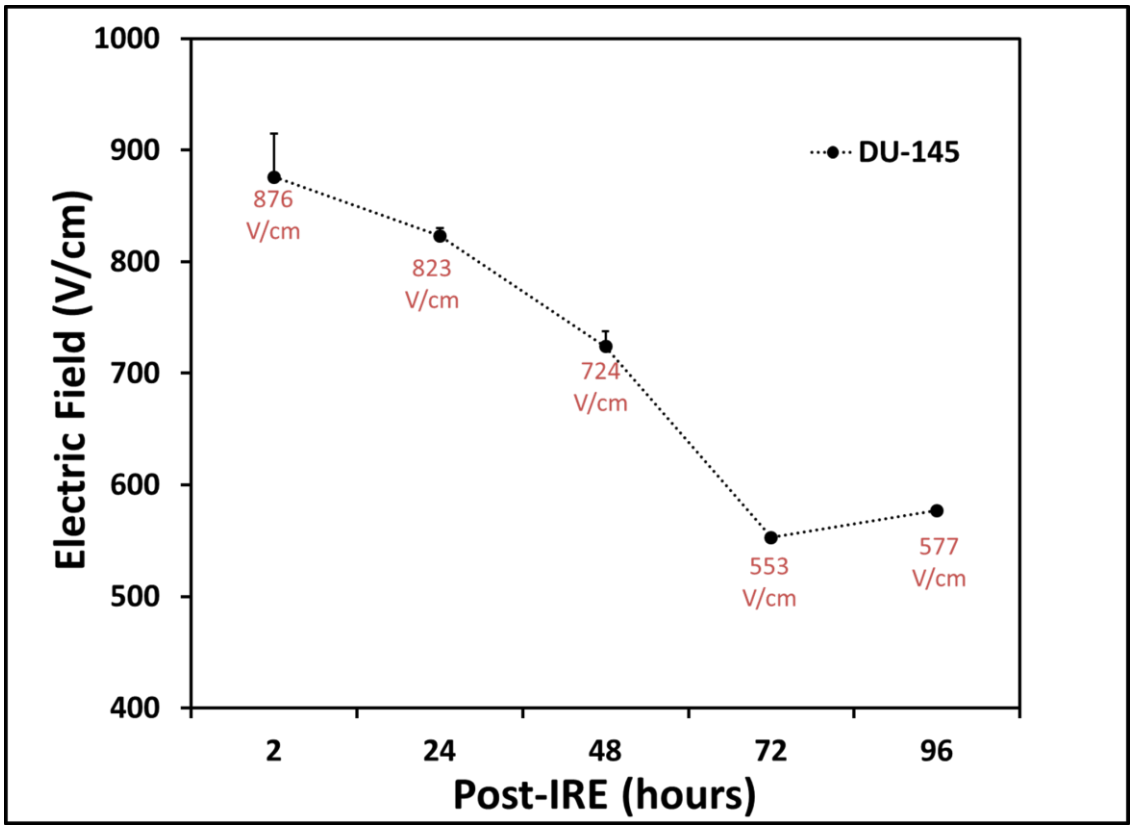

Figure 15: The electric field threshold for cell death of DU-145 cells

The overall electric field threshold for cell death for DU-145 was determined by averaging the time points at which the lesion was fully developed, 48-96 hrs. This overall threshold was determined to be 618 V/cm, and as was done for the PC-3 cell line, numerical modeling confirmed experimental results. Figure 16 shows the DU-145 threshold for cell death determined from numerical modeling overlaid on a hydrogel.

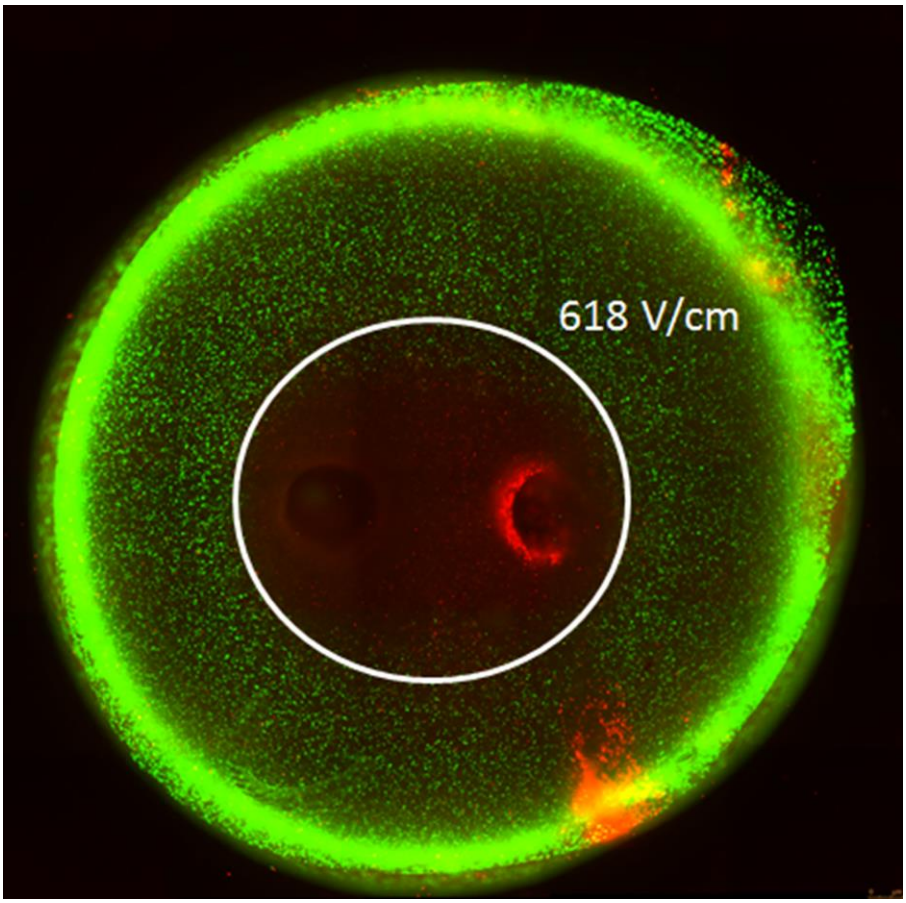

Figure 16: DU-145 electric field threshold for cell death overlaid on a hydrogel

Actin and nuclei staining using confocal microscopy as well as scanning electron microscopy were chosen to investigate the behavior of the cells within the hydrogel model to determine cytoskeleton structure as well as the effect of IRE pulse delivery. The results from both of these trials determined whether the variability in electric field thresholds for cell death as well as corresponding lesion areas for certain cell lines was due to cytoskeleton structure within the

collagen I environment. As described in the methods section, cells were stained with rhodamine phalloidin and DAPI to visualize actin filaments and nuclei for confocal microscopy. The nuclei of both PC-3 and DU-145 cells appeared spherical in untreated regions of the hydrogel with large amounts of actin surrounding them. As seen in Figure 17, PC-3 cells remained as individual cells while DU-145 cells tended to aggregate into large clusters. The clusters of DU-145 cells could explain the variability between trials, as clusters of cells experience different effects due to pulsed electric fields. For high electric fields, clusters of cells become electrically insulated, and therefore, are electroporated as individual cells, however, for lower electric fields, cells in clusters behave as one large cell as they are considered electrically conductive [15, 38, 39]. The mechanism behind electroporation on the molecular level is not well understood, but it seems that the clusters of DU-145 cells are electroporated as individual cells when experiencing irreversible electric fields. Additionally, it has been shown that clusters of cells are harder to electroporate, generally requiring higher pulsing parameters than single cells, as the random orientation of cell boundaries within clusters are affected differently by applied electric fields [40].

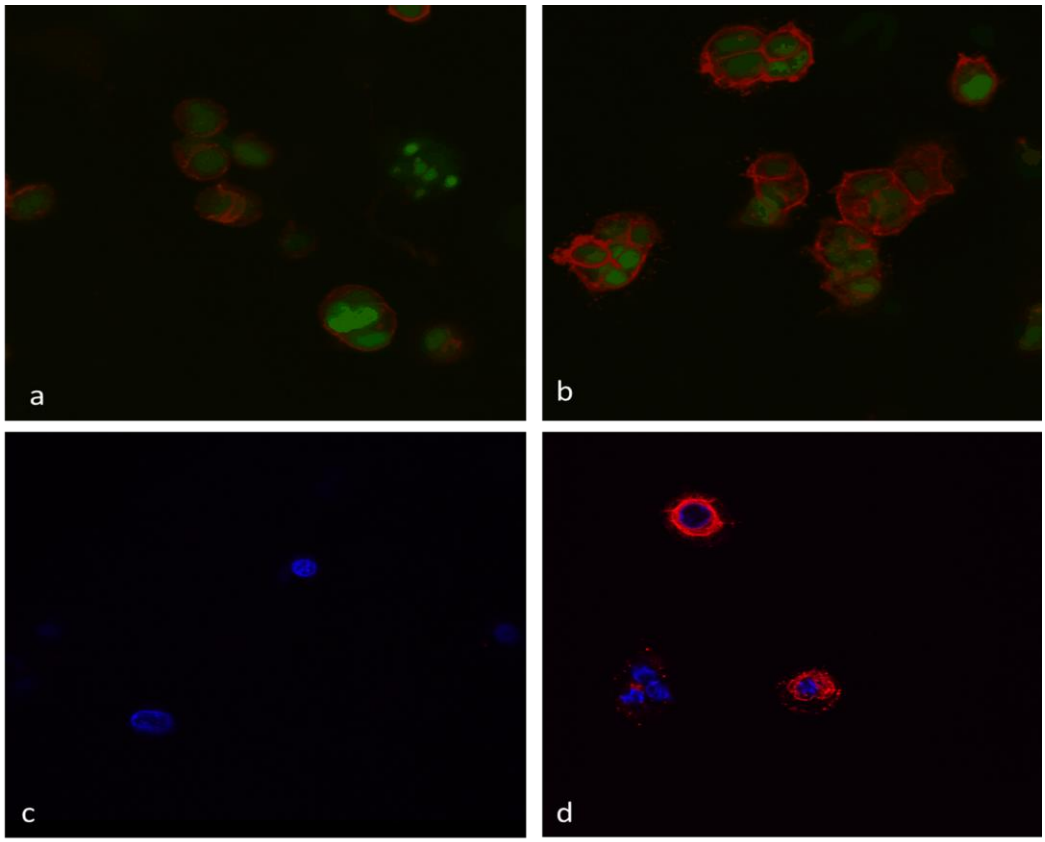

Figure 17: Actin and nuclei staining in PC-3 and DU-145 cells. Untreated PC-3 (a) and DU-145 (b) display abundant actin staining surrounding the nuclei, whereas actin degradation can be detected in PC-3 (c) and DU-145 (d) treated cells.

For both cell lines, IRE pulse delivery resulted in degradation of the actin cytoskeleton. Reversible electroporation also degrades the actin cytoskeleton, however, the cytoskeleton has been shown to recover unlike irreversible electroporation [41, 42] . Additionally, the degree of degradation seems to be dependent upon pulsing parameters, particularly applied voltage, and differs between cell lines [42]. This could explain the time it takes for the lesion areas to become fully developed. Furthermore, actin and DNA staining was performed after 24 hours as well as 3 days of culturing cells in the hydrogel with no difference seen in the shape or amount of actin present, indicating that the cells were attached by 24 hours.

Scanning electron microscopy (SEM) of the hydrogels seeded with cells were imaged using an environmental SEM as previously described in methods. Samples were initially prepared by freeze drying prior to imaging, however, the freeze drying process affects the structure and viability of cells within the hydrogel. The drying process resulted in some cracked areas in the hydrogel (Figure 18), and, therefore, to verify that artifacts of the drying process were not being seen, wet samples of the hydrogels were also imaged. Adjusting humidity, temperature, and pressure allowed some of the water to dry out of the sample in order to visualize the cells in the hydrogel. The wet samples produced better images than the freeze dried samples in which cells

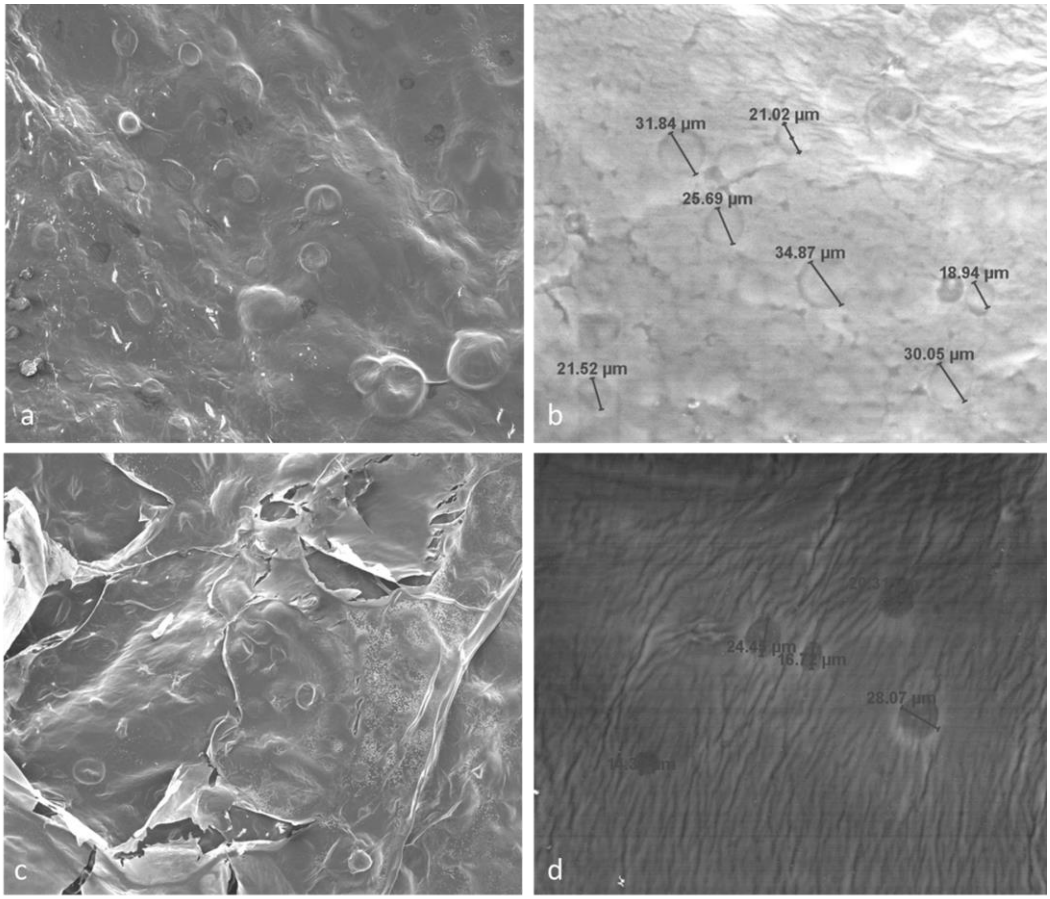

Figure 18: ESEM images of PC-3 and DU-145 cells in hydrogel. a) PC-3 cells in a freeze dried sample at 250x; b) wet sample at 70% humidity and 750x. c) DU-145 cells in a freeze dried sample at 250x; d) wet sample at 80% humidity and 750x

appeared spherical and when measured were larger than cells in suspension indicating that the cells were spreading out in a more i*n vivo* like manner than traditional cell suspension studies. In cell suspension, PC-3 cells were on average, 18.08 μm in diameter but in the hydrogel they were averaged to be about 26.28 μm. DU-145 cells had an average diameter of 16.91 μm in cell suspension, but were 20.77 μm in the hydrogel model. Similar results were seen in pancreatic cancer cells which will be discussed in the next section.

4.3 Pancreatic Cancer Cell Death Characterization in the Hydrogel Model

Two human pancreatic cancer cell lines, PANC-1 and BxPC-3, were used to determine the electric field threshold for cell death in the hydrogel model. PANC-1 cells exhibited similar results to PC-3 cells while BxPC-3 thresholds were more consistent with results seen in the DU-145 cells. Lesion areas were visualized using a live/dead assay as was done for prostate cancer cells, correlating experimental and numerical lesion widths to back out the electric field threshold for cell death. Additionally, cytoskeleton structure was demonstrated through confocal imaging of actin and nuclei staining as well as scanning electron microscopy. The next sections will expand upon the results from these two cell lines.

4.3.1 PANC-1 Cell Death Characterization

As hypothesized, the electric field threshold for cell death of PANC-1 cells was within the anticipated 500-600 V/cm. The overall electric field threshold for cell death was lower than that of PC-3 cells and for some trials was in the 450-500 V/cm range even though the overall average was within the hypothesized range. Similar to prostate cancer cells, the lesion area was larger

with higher applied voltages as increasing certain pulse parameters including applied voltage lead to greater amounts of electroporation. The lesion area over time grew for the PANC-1 cells between 2 and 24 hours post-IRE pulse delivery, unlike in the PC-3 cell line. The lesion was not fully developed until 24 hours at which time lesion areas remained consistent with later time points as seen in Figure 19. It is noted that for the second trial of PANC-1 cells, the lesion area was not sufficiently established 2 hours post-IRE delivery for experimental measurements of the length and width to be taken. Therefore, the electric field could not be determined for that particular time point. The electric field thresholds for cell death for the PANC-1 cell line were determined as 514 V/cm, 489 V/cm, and 456 V/cm for the three sets of experiments.

For the first trial of PANC-1 cells the threshold for cell death was determined as 608 ± 162 V/cm

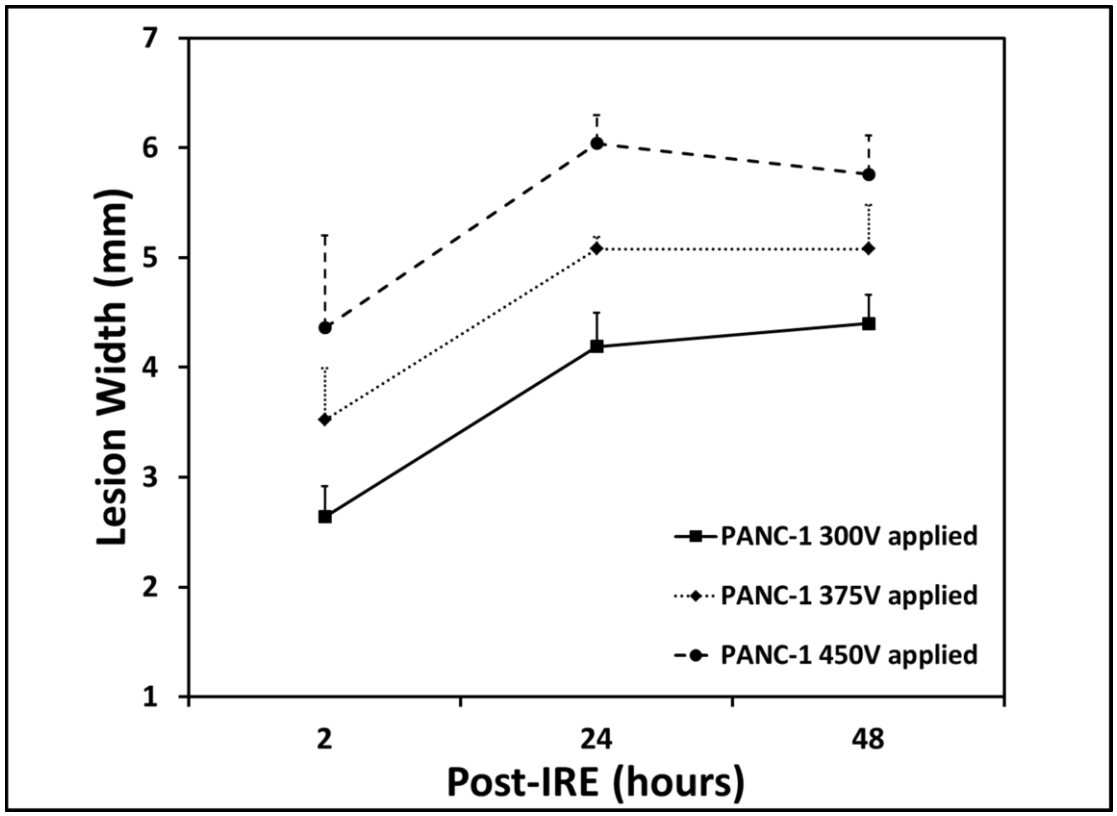

Figure 19: The lesion width vs time for PANC-1 cells.

when averaged over all time points. The lesion area did not fully develop until 24 hours, and; therefore, the electric field threshold for cell death is taken as the average over the 24 and 48 hour analysis time points giving a threshold of 514 ± 5 V/cm. Additionally, the lesion widths grew with increasing voltage, as was seen with previous cell lines. For 300V applied, the lesion width was 3.48 mm, 4.30 mm at 375V applied and 5.04 mm at 450V applied for the first trial. The second trial showed a similar threshold of 489 ± 8 V/cm averaged over the 24 and 48 hour time points as measurements of lesion width were not taken for the 2 hour time point due to an unconnected lesion area. For this trial, lesion widths were 4.33 mm, 5.04 mm, and 5.82 mm for 300V, 375V, and 450V applied, respectively. The threshold for the third trial remained within the 500-600 V/cm for the overall threshold at 522 ± 114V/cm, but the 24 and 48 hour averaged threshold was between 450V/cm and 500 V/cm at 456 ± 12 V/cm. Lesion widths measured 3.98 mm, 4.85 mm, and 5.79 mm for 300V, 375V, and 450V applied, averaged over time points. PANC-1 cells were larger than the prostate cancer cells which made them easier to kill using IRE and therefore, accounts for this slightly lower electric field threshold.

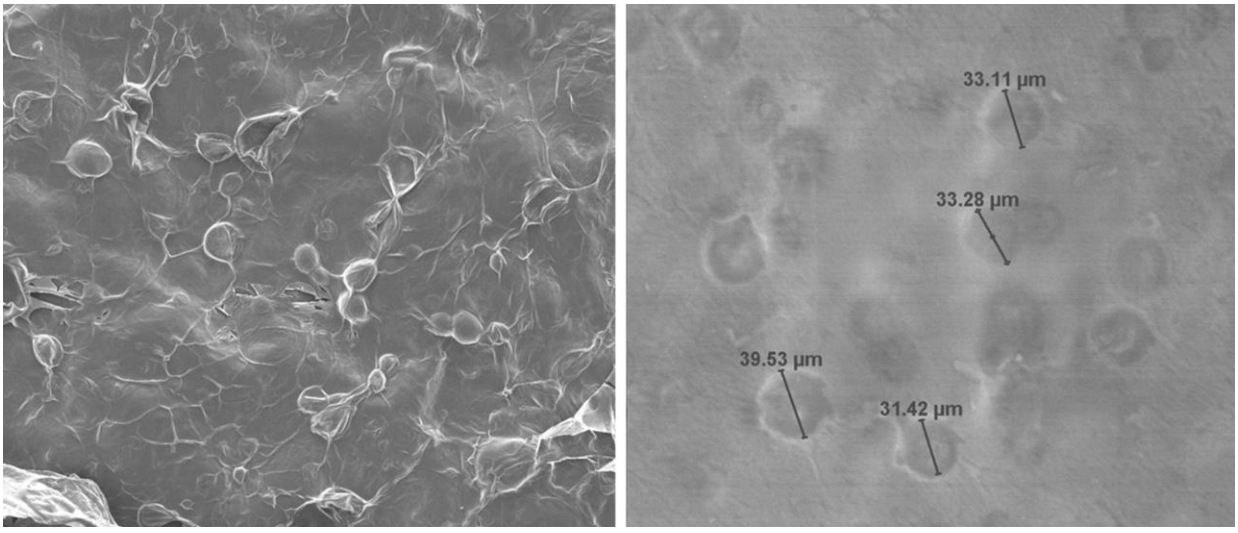

Figure 20: SEM images of PANC-1 cells. The left image was prepared by freeze drying and imaging at 250x while the right is a wet sample with measurements at 60% humidity and 750x magnification.

In cell suspension, PANC-1 cells were 17.29 μm in diameter on average while in the hydrogel model they were 34.34 μm in diameter as was seen from SEM images in Figure 20. The SEM images of the cell showed them as spherical, but the larger size indicated they were spreading out and attaching to the collagen I matrix. Confocal imaging of the actin cytoskeleton reinforced this as plentiful amounts of actin can be seen surrounding the nucleus of the cells (Figure 21) similar to what was seen for PC-3 cells.

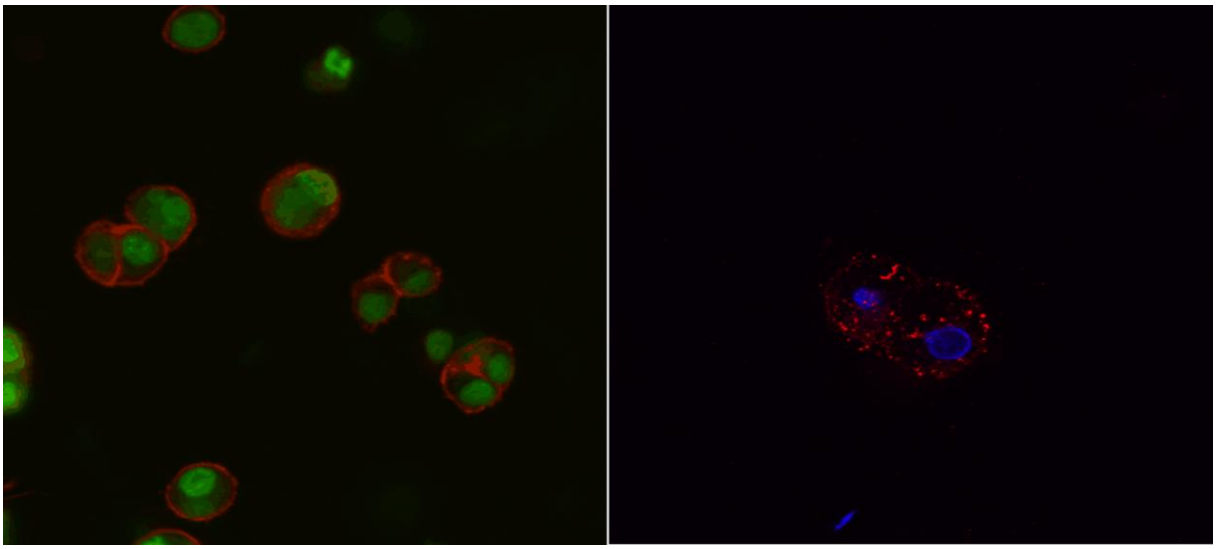

Figure 21: Confocal microscopy images of actin (red) and DNA (green on the left and blue on the right) staining in PANC-1 cells. The left shows the actin cytoskeleton in healthy PANC-1 cells while the right shows actin degradation in electroporated PANC-1 cells.

An additional trial of experiments was run for the PANC-1 cells to determine whether the lesion area became fully developed at a time point before 24 hours. This additional trial followed the same procedure with analysis time points at 2, 6, and 12 hours post-IRE. The lesion was still developing at 2 and 6 hours, but was fully developed by 12 hours with an electric field threshold of 466 ± 16 V/cm. Figure 22 shows the electric field distribution over the different time points indicating that the lesion was fully developed after 12 hours as the electric field thresholds remain similar for 12, 24, and 48 hours post-IRE. Therefore, it can be concluded that the optimal

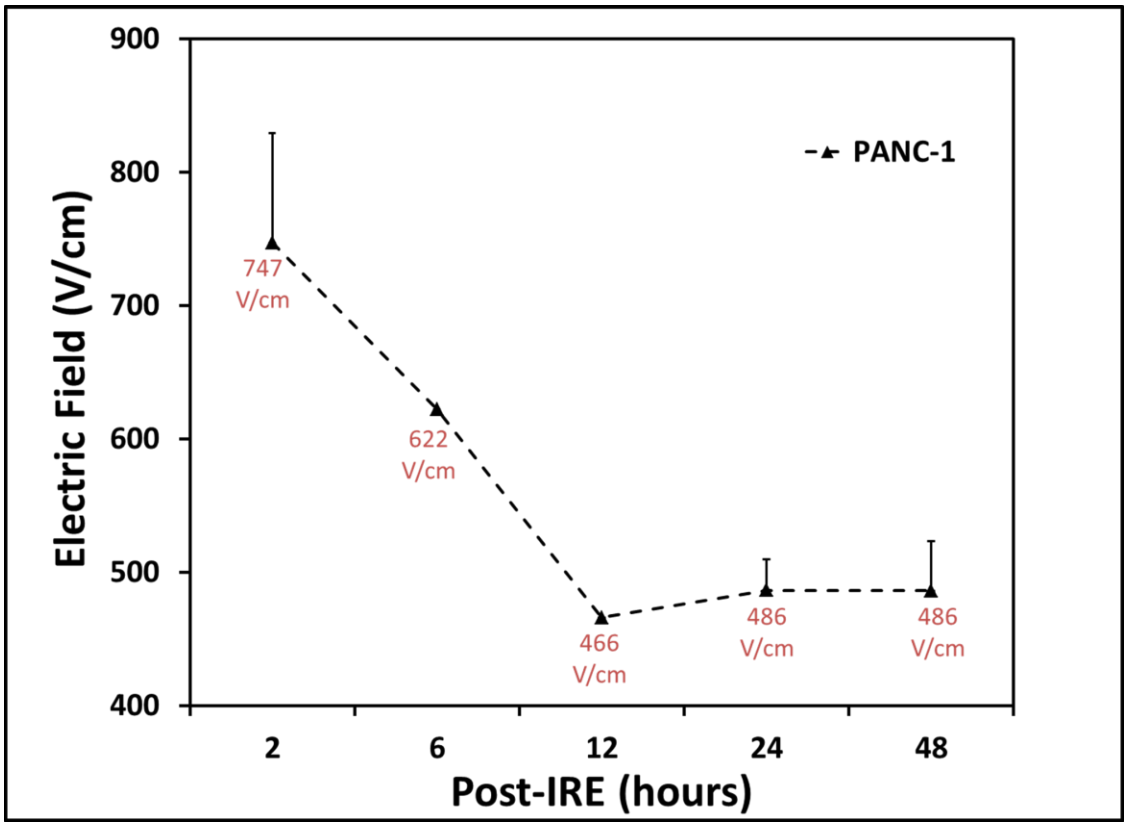

Figure 22: The electric field threshold for cell death vs time for PANC-1 cells.

time for analysis for the PANC-1 cells was at least 12 hours post-IRE pulse delivery. Additionally, the overall electric field threshold for cell death for the PANC-1 cells was determined as the average of the thresholds for 12, 24, and 48 hours post-IRE. Figure 23 shows this overall PANC-1 threshold of 479 V/cm superimposed on a hydrogel image stained with calcein AM and propidium iodide.

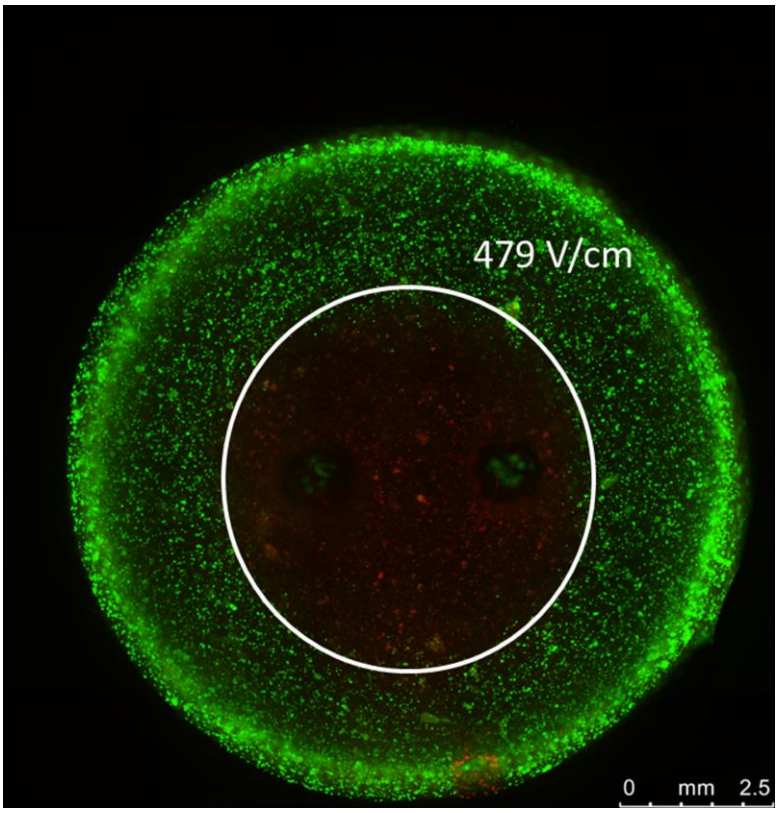

Figure 23: PANC-1 electric field threshold for cell death overlaid on a hydrogel

4.3.2 BxPC-3 Cell Death Characterization

Similar to the DU-145 cell line, the second pancreatic cell line, BxPC-3, had more variability in the results and did not fall within the anticipated 500-600 V/cm threshold range. The BxPC-3 cell line formed cell clusters with similar electric field thresholds for cell death as the second prostate cancer cell line, DU-145. The first trial for BxPC-3 cells resulted in an electric field threshold of 878 ± 10 V/cm. The lesion area was not fully developed until 24 hours with no measurement taken at 2 hours post-IRE as the lesion was not developed enough to measure accurate lesion dimensions. The lesion area was larger with greater applied voltage as has been seen with the other three cell lines (Figure 24). Lesion widths measured 1.95 mm for 300V applied, 2.81 mm for 375V applied, and 3.52 mm for 450V applied. Additionally, the second trial of BxPC-3 cells showed similar trends with the lesion becoming fully developed at 24 hours

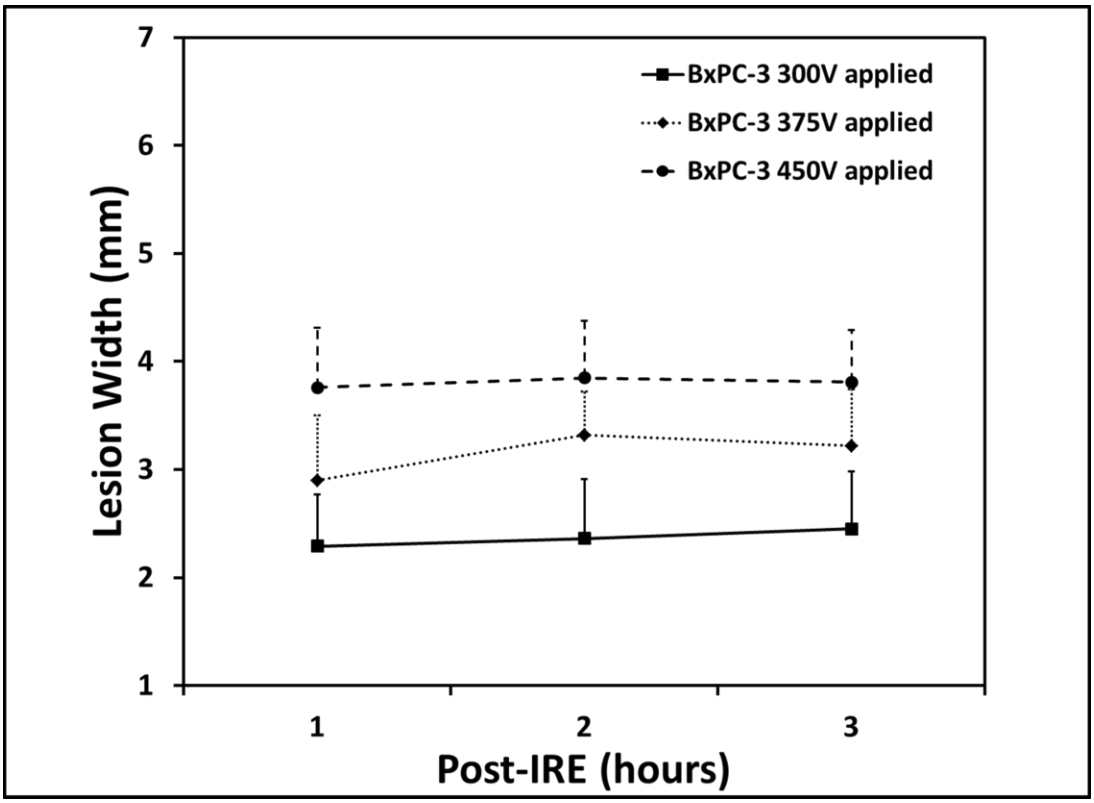

Figure 24: The lesion width vs time for the pancreatic cancer cell line, BxPC-3.

with an electric field threshold averaged over 24 and 48 hours post-IRE pulse delivery of 682 ± 5 V/cm. For this trial, the lesion width for 300V applied was 2.87 mm, 3.57 mm for 375V applied, and 4.32 mm for 450V applied. A third trial for the BxPC-3 cells showed the lesion to be fully developed by 24 hours with an overall electric field threshold for all time points of 853 ± 56 V/cm, and an electric field threshold for cell death over the 24 and 48 hour time points of 821 ± 7 V/cm. Lesion widths measured 2.17 mm, 3.02 mm, and 3.51 mm for 300V, 375V, and 450V applied, respectively. Figure 25 shows the electric field thresholds over time for the BxPC-3 cells.

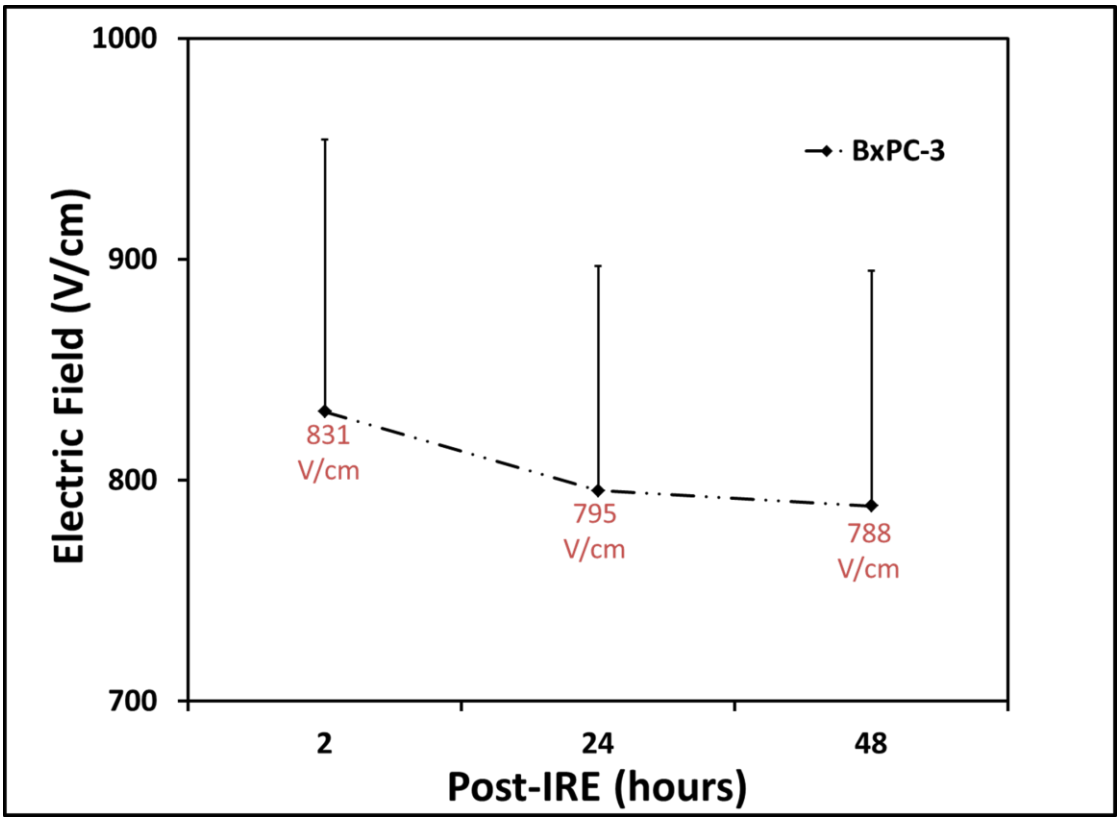

Figure 25: The electric field threshold for cell death vs time for the pancreatic cell line, BxPC-3.

As was done for the previous 3 cell lines, the overall electric field threshold for cell death for the BxPC-3 cell line was taken as an average of the thresholds determined for fully developed lesions. Therefore, for the BxPC-3 cells, the overall threshold was 792 V/cm which is the average of thresholds after 24 hours post-IRE as the lesion was fully developed by 24 hours. This threshold is seen overlaid on a hydrogel image in Figure 26.

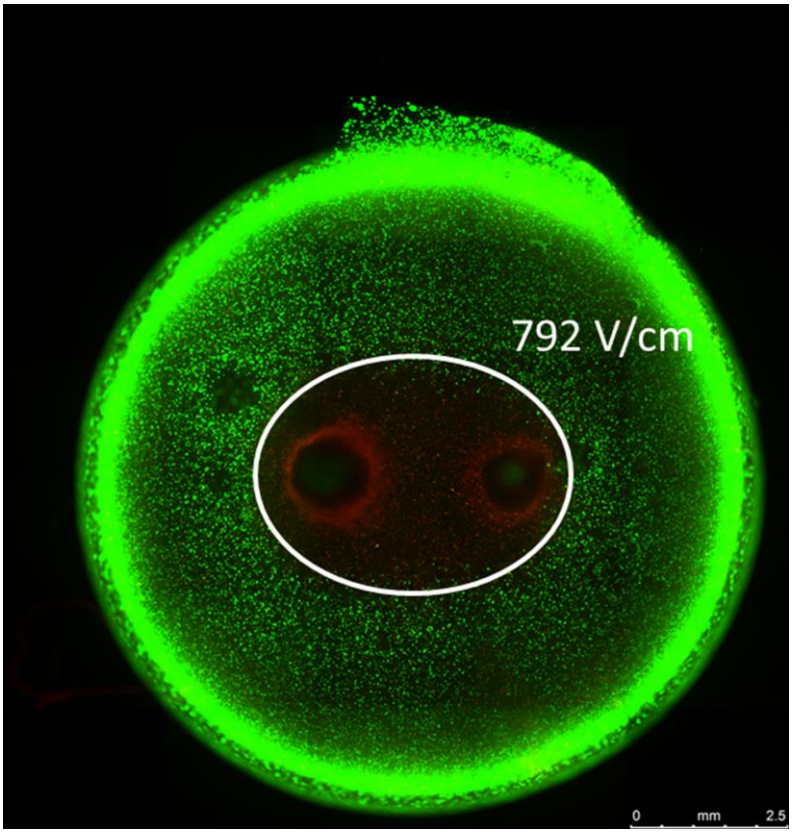

Figure 26: BxPC-3 electric field threshold for cell death overlaid on a hydrogel

Confocal microscopy of actin and DNA staining and scanning electron microscopy were also used to assess the cytoskeleton of the pancreatic cancer cells to ensure cells were attaching to the matrix in a more i*n vivo* like manner than cell suspension. As seen in Figure 27 there is sufficient actin cytoskeleton surrounding the BxPC-3 nuclei which appear spherical in the collagen I matrix. SEM of the hydrogels seeded with BxPC-3 cells showed spherical cells with average diameters of 22.85 μm. The diameters of the cells seen in the hydrogels were larger than the average diameter of 16.10 μm in cell suspension. Therefore, this indicated the cells were complacent in the collagen I matrix and were attaching to that matrix, spreading out in an *in vivo* like manner. Additionally, from the confocal images (Figure 27), the BxPC-3 cells formed cell clusters much like the DU-145 cells which could explain why their threshold were so much higher than the other pancreatic cell line, PANC-1.

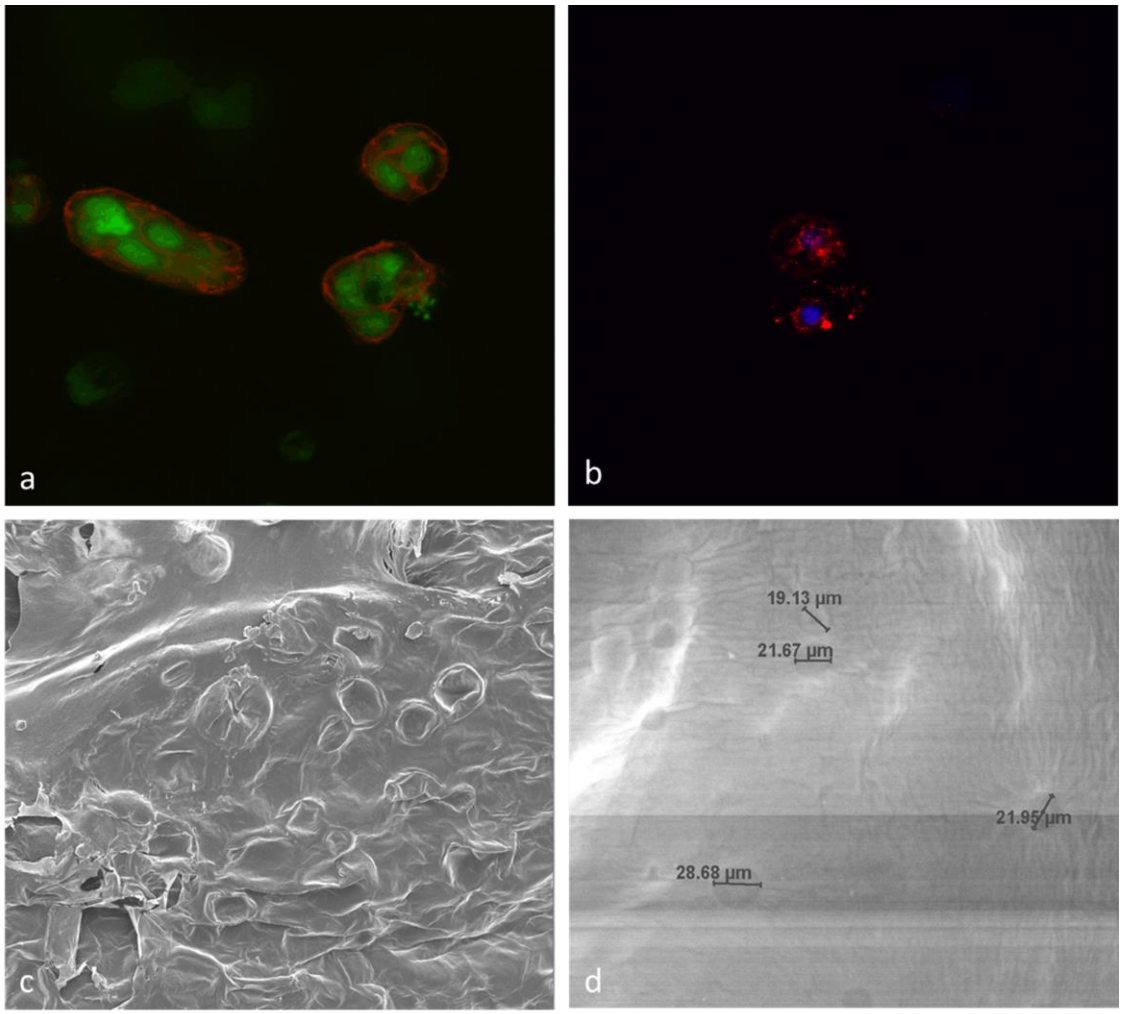

Figure 27: Actin and nuclei staining of BxPC-3 cells can be seen in healthy cells a) and electroporated cells b). SEM images of the cells can be seen in a freeze dried sample at 250x (c) and in a wet sample at 80% humidity and 750x magnification (d).

Chapter 5: Discussion and Future Work

Pancreatic and prostate cancer are both detrimental diseases affecting thousands of people annually. Pancreatic cancer has the fourth leading death rate among cancers with low survival rates and few effective treatment options as the disease is usually not diagnosed until late, aggressive stages. While prostate cancer has high survival rates and is less aggressive than pancreatic cancer, it is the most common cancer in men and advanced stages can present challenges as well. The anatomy of both cancers limits resection of tumors as well as thermal based treatment options such as radiofrequency ablation due to close proximity to critical structures, blood vessels, and nerves. New therapies such as irreversible electroporation are needed to treat these cancers. The thresholds necessary to kill pancreatic and prostate cancer cells have not been previously investigated. The hydrogel model is a cheaper, preliminary model to investigate the thresholds for cell death with benefits over cell suspension studies as cells behave in a more *in vivo* like manner. Additionally, it offers benefits over tissue and animal models as the bulk conductivity change in the hydrogel is assumed to be zero, simplifying Laplace's equation, allowing the electric field threshold to be determined without the extra challenge of estimating the change in conductivity. Future work can then incorporate the thresholds determined from the hydrogel model into tissue or animal models to determine the bulk change in conductivity for various tissues.

The hydrogel model was successfully used to determine the irreversible electroporation thresholds for cell death for prostate and pancreatic cancer cell lines. It was initially expected that the irreversible electroporation thresholds for cell death for the two pancreatic and prostate cancer cell lines would fall within a 500-600V/cm range as this is what has been seen in literature for other models. However, there was some variation in thresholds due to differences between cell lines as can be seen in Table 1. The overall electric field thresholds for cell death were determined at the times when the lesions had become fully developed which varied between cell lines. Additionally, the thresholds varied due to differences in cell size as larger cells are easier to kill, and therefore, require lower electric field thresholds. Confocal imaging of actin cytoskeleton and SEM images of the cells were used to better understand how the cells were behaving in the collagen I of the hydrogel. It was found for all cell lines that cells had a

Table 1: Summary of characteristics and results for prostate and pancreatic cancer cell lines

Cell Line	Tissue and Disease	Derivation	Cell Suspension Average Diameter (µm)	Hydrogel Average Cell Diameter (µm)	Electric Field Threshold for Cell Death (V/cm) n=3	Time Post-IRE for lesion to fully develop (hrs)
PC-3	Human prostate grade IV adenocarcinoma	Bone metastasis	18.08 ± 0.31 (n=10)	26.28 ± 6 (n=7)	541 ± 2	~2
DU-145	Human prostate carcinoma	Brain metastasis	16.91 ± 0.26 (n=7)	20.77 ± 6 (n=5)	618 ± 93	~48
PANC-1	Human pancreatic carcinoma	Primary tumor	17.29 ± 0.45 (n=10)	34.34 ± 4 (n=4)	479 ± 12	~12
BxPC-3	Human pancreatic adenocarcinoma	Primary tumor	16.10 ± 0.54 (n=8)	22.85 ± 4 (n-4)	792 ± 5	~24

larger average diameter in the hydrogel than in suspension, indicating that cells were behaving in a more *in vivo* like manner and actively attaching to the collagen I matrix.

For the PC-3, prostate cancer cell line all three trials indicated an electric field threshold for cell death between 500 and 600 V/cm with a fully developed lesion two hours post-IRE. An additional prostate cancer cell line, DU-145, was also investigated which resulted in larger electric field thresholds ranging between 600 and 700 V/cm with the lesion fully developed 48 hours post-IRE. SEM and confocal images of the cell lines showed DU-145 cells to have a smaller diameter than PC-3 cells and DU-145 cells tended to form clusters of cells, both of which require a higher electric field threshold to result in cell death which was seen experimentally.

For PANC-1, pancreatic cancer cell line, the threshold for cell death was close to 500V/cm, with the lesion reaching fully size 24 hours post-IRE. The PANC-1 cells were larger than both prostate cancer cell lines attributing to the smaller threshold necessary to kill them. An additional pancreatic cancer cell line, BxPC-3, was studied and required a higher threshold than the PANC-1 cells as well as the prostate cell lines. Confocal imaging of actin cytoskeleton showed the BxPC-3 cells formed clusters of cells in the hydrogel while SEM images showed the cells to be larger in the hydrogel than cell suspension indicating they were acting in an *in vivo* manner. However, as seen in Table 1, the BxPC-3 cells had a smaller diameter than PANC-1 cells which required a higher threshold in the 700-800V/cm range to kill the cells. Additionally, similar to the first pancreatic cancer cell line, lesions for the BxPC-3 cells were not fully developed until 24 hours post-IRE.

Therefore, the results indicate that different cell lines will behave differently in a collagen I matrix, and require varying electric field thresholds for cell death. It was concluded that cell lines that tend to form large clusters of cells generally require a higher threshold to achieve cell death, while individual cells or those forming much smaller clusters can be killed with lower thresholds. Additionally, larger cells are easier to kill requiring lower electric field thresholds than smaller cells. This is important information that will be helpful in treatment planning models to better optimize IRE treatments.

Future work should involve the transition to *in vivo* or *ex vivo* trials of pancreatic and prostate tissue to validate the electric field thresholds seen *in vitro* as well as to determine whether the thresholds will hold in heterogeneous tissue. Furthermore, the thresholds determined from the hydrogel model can be used *in vivo* or *ex vivo* to determine the change in conductivity for tissues. After thresholds are determined i*n vivo*, they can then be applied to treatment planning softwares to optimize prostate and pancreatic cancer treatment with IRE as well as to improve the acceptance of IRE as a mainstream cancer therapy.

References:

1. *Cancer Facts & Figures 2013*. Atlanta: American Cancer Society.
2. *Pancreatic Cancer*. National Cancer Institute, 2013.
3. José, A., et al., *Irreversible electroporation shows efficacy against pancreatic carcinoma without systemic toxicity in mouse models.* Cancer Letters, 2012. **317**(1): p. 16-23.
4. *Prostate Cancer* National Cancer Institute, 2013.
5. Davalos, R. and B. Rubinsky, *Tissue ablation with irreversible electroporation*, U.S.P.a.T. Office, Editor 2006.
6. Garcia, P.A., et al., *Non-thermal irreversible electroporation (N-TIRE) and adjuvant fractionated radiotherapeutic multimodal therapy for intracranial malignant glioma in a canine patient.* Technol Cancer Res Treat, 2011. **10**(1): p. 73-83.
7. Rubinsky, B., G. Onik, and P. Mikus, *Irreversible electroporation: a new ablation modality--clinical implications.* Technol Cancer Res Treat, 2007. **6**(1): p. 37-48.
8. Onik, G., P. Mikus, and B. Rubinsky, *Irreversible electroporation: implications for prostate ablation.* Technol Cancer Res Treat, 2007. **6**(4): p. 295-300.
9. Joshi, R.P. and K.H. Schoenbach, *Mechanism for membrane electroporation irreversibility under high-intensity, ultrashort electrical pulse conditions.* Phys Rev E Stat Nonlin Soft Matter Phys, 2002. **66**(5 Pt 1): p. 052901.
10. Gissel, H., *Electroporation and Cellular Physiology*, 2011, Springer New York: New York, NY. p. 9-17.
11. Kotnik, T., et al., *Cell Membrane Electroporation-Part 1: The Phenomenon.* IEEE ELECTRICAL INSULATION MAGAZINE, 2012. **28**(5): p. 14-23.
12. Neu, J.C. and W. Krassowska, *Asymptotic model of electroporation.* Phys. Rev. E, 1999. **59**(3): p. 3471-82.
13. DeBruin, K.A. and W. Krassowska, *Modeling electroporation in a single cell. I. Effects of field strength and rest potential.* Biophys J, 1999. **77**(3): p. 1213-24.
14. Glaser, R.W., et al., *Reversible electrical breakdown of lipid bilayers: formation and evolution of pores.* Biochim Biophys Acta, 1988. **940**(2): p. 275-87.
15. Kotnik, T., G. Pucihar, and D. Miklavčič, *Induced Transmembrane Voltage and Its Correlation with Electroporation-Mediated Molecular Transport.* The Journal of membrane biology, 2010. **236**(1): p. 3-13.
16. Kotnik, T., *The Cell in the Electric Field*, 2011, Springer New York: New York, NY. p. 19-29.
17. Dev, S.B., D. Dhar, and W. Krassowska. *Electric field of a six-needle array electrode used in drug and DNA delivery in vivo: analytical versus numerical solution*. United States: Institute of Electrical and Electronics Engineers, Inc.
18. Corović, S., M. Pavlin, and D. Miklavcic, *Analytical and numerical quantification and comparison of the local electric field in the tissue for different electrode configurations.* Biomedical engineering online, 2007. **6**(1): p. 37-37.
19. Arena, C.B., et al., *A three-dimensional in vitro tumor platform for modeling therapeutic irreversible electroporation.* Biophysical journal, 2012. **103**(9): p. 2033-2042.
20. Hamilton, W.A. and A.J. Sale, *Effects of high electric fields on microorganisms. 2. Mechanism of action of the lethal effect.* Biochimica et Biophysica Acta (BBA), 1967. **163**: p. 37-43.

21. Crowley, J.M., *Electrical breakdown of biomolecular lipid membranes as an electromechanical instability.* Biophysical Journal, 1973. **13**: p. 711-724.
22. Zimmermann, U., G. Pilwat, and F. Riemann, *Dielectric breakdown of cell membranes.* Biophys J, 1974. **14**(11): p. 881-99.
23. Neumann, E. and K. Rosenheck, *Permeability changes induced by electric impulses in vesicular membranes.* J. Membrane Biol., 1972. **10**: p. 279-290.
24. Edd, J.F., et al. *In vivo results of a new focal tissue ablation technique: irreversible electroporation*.
25. Miklavcic, D., et al., *A validated model of in vivo electric field distribution in tissues for electrochemotherapy and for DNA electrotransfer for gene therapy.* Biochim Biophys Acta, 2000. **1523**(1): p. 73-83.
26. Sano, M., et al., *Towards the creation of decellularized organ constructs using irreversible electroporation and active mechanical perfusion.* BioMedical Engineering OnLine, 2010. **9**(1): p. 83.
27. Garcia, P.A., et al., *Intracranial nonthermal irreversible electroporation: In vivo analysis.* J Membr Biol, 2010. **236**(1): p. 127-136.
28. Neal Ii, R.E., et al., *Treatment of breast cancer through the application of irreversible electroporation using a novel minimally invasive single needle electrode.* Breast Cancer Research and Treatment, 2010. **123**(1): p. 295-301.
29. Ball, C., K.R. Thomson, and H. Kavnoudias, *Irreversible electroporation: a new challenge in "out of operating theater" anesthesia.* Anesth Analg, 2010. **110**(5): p. 1305-9.
30. Thomson, K.R., et al., *Investigation of the Safety of Irreversible Electroporation in Humans.* Journal of Vascular and Interventional Radiology, 2011. **22**(5): p. 611-621.
31. Kingham, T.P., et al., *Ablation of perivascular hepatic malignant tumors with irreversible electroporation.* Journal of the American College of Surgeons, 2012. **215**(3): p. 379-387.
32. Cannon, R., et al., *Safety and early efficacy of irreversible electroporation for hepatic tumors in proximity to vital structures.* J Surg Oncol, 2013. **107**(5): p. 544-9.
33. Bagla, S. and D. Papadouris, *Percutaneous irreversible electroporation of surgically unresectable pancreatic cancer: a case report.* Journal of vascular and interventional radiology : JVIR, 2012. **23**(1): p. 142-145.
34. Onik, G. and B. Rubinsky, eds. *Irreversible Electroporation: First Patient Experience Focal Therapy of Prostate Cancer*. Irreversible Electroporation, ed. B. Rubinsky2010, Springer Berlin Heidelberg. 235-247.
35. Szot, C.S., et al., *3D in vitro bioengineered tumors based on collagen I hydrogels.* Biomaterials, 2011. **32**(31): p. 7905-7912.
36. Al-Sakere, B., et al., *Tumor ablation with irreversible electroporation.* PLoS ONE, 2007. **2**(11): p. e1135.
37. Breton, M. and L.M. Mir, *Microsecond and nanosecond electric pulses in cancer treatments.* Bioelectromagnetics, 2012. **33**(2): p. 106-123.
38. Pucihar, G., D. Miklavcic, and T. Kotnik, *A Time-Dependent Numerical Model of Transmembrane Voltage Inducement and Electroporation of Irregularly Shaped Cells.* IEEE Transactions on Biomedical Engineering, 2009. **56**(5): p. 1491-1501.

39. Pucihar, G., T. Kotnik, and D. Miklavcic, *An experimental and numerical study of the induced transmembrane voltage and electroporation on clusters of irregularly shaped cells*, 2007, Springer Berlin Heidelberg: Berlin, Heidelberg. p. 639-642.
40. Joshi, R.P., A. Mishra, and K.H. Schoenbach. *Model Assessment of Cell Membrane Breakdown in Clusters and Tissues Under High-Intensity Electric Pulsing*. PISCATAWAY: IEEE.
41. Kanthou, C., et al., *The endothelial cytoskeleton as a target of electroporation-based therapies.* Mol Cancer Ther, 2006. **5**(12): p. 3145-52.
42. Pehlivanova, V.N., I.H. Tsoneva, and R.D. Tzoneva, *Multiple effects of electroporation on the adhesive behaviour of breast cancer cells and fibroblasts.* Cancer cell international, 2012. **12**(1): p. 9-9.